

AD--A169 942

AFGL-TR-85-0342  
ENVIRONMENTAL RESEARCH PAPERS, NO. 943

Balloon-Borne, High Altitude Gravimetry  
The Flight of DUCKY Ia (11 October 1983)

ANDREW R. LAZAREWICZ  
BRENDA J. SCHILINSKI  
RALPH J. COWIE  
CATHERINE L. RICE  
PETER MOSS  
LEONARD N. CARTER

DTIC  
ELECTE  
JUL 24 1986  
S D  
D



31 December 1985



Approved for public release; distribution unlimited.

DTIC FILE COPY



EARTH SCIENCES DIVISION

PROJECT 7600

**AIR FORCE GEOPHYSICS LABORATORY**

HANSCOM AFB, MA 01731

86 7 23 008

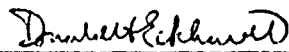
IN-HOUSE REPORTS

This technical report has been reviewed and is approved for publication.

  
\_\_\_\_\_  
ANDREW R. LAZAREWICZ  
Contract Manager

  
\_\_\_\_\_  
THOMAS P. ROONEY  
Chief, Geodesy & Gravity Branch

FOR THE COMMANDER

  
\_\_\_\_\_  
DONALD H. ECKHARDT  
Director  
Earth Sciences Division

This report has been reviewed by the ESD Public Affairs Office (PA) and is releasable to the National Technical Information Service (NTIS).

Qualified requestors may obtain additional copies from the Defense Technical Information Center. All others should apply to the National Technical Information Service.

If your address has changed, or if you wish to be removed from the mailing list, or if the addressee is no longer employed by your organization. please notify AFGL/DAA, Hanscom AFB, MA 01731. This will assist us in maintaining a current mailing list.

Unclassified

SECURITY CLASSIFICATION OF THIS PAGE

REPORT DOCUMENTATION PAGE					
1a. REPORT SECURITY CLASSIFICATION Unclassified		1b. RESTRICTIVE MARKINGS N/A			
2a. SECURITY CLASSIFICATION AUTHORITY		3. DISTRIBUTION/AVAILABILITY OF REPORT Approved for public release; distribution unlimited			
2b. DECLASSIFICATION/DOWNGRADING SCHEDULE					
4. PERFORMING ORGANIZATION REPORT NUMBER(S) AFGL-TR-85-0342 ERP, No. 943		5. MONITORING ORGANIZATION REPORT NUMBER(S)			
6a. NAME OF PERFORMING ORGANIZATION Air Force Geophysics Laboratory	6b. OFFICE SYMBOL (If applicable) AFGL/LWG	7a. NAME OF MONITORING ORGANIZATION			
6c. ADDRESS (City, State and ZIP Code) Hanscom AFB Massachusetts 01731		7b. ADDRESS (City, State and ZIP Code)			
8a. NAME OF FUNDING/SPONSORING ORGANIZATION	8b. OFFICE SYMBOL (If applicable)	9. PROCUREMENT INSTRUMENT IDENTIFICATION NUMBER			
8c. ADDRESS (City, State and ZIP Code)		10. SOURCE OF FUNDING NOS.			
		PROGRAM ELEMENT NO.	PROJECT NO.	TASK NO.	WORK UNIT NO.
11. TITLE (Include Security Classification) Balloon-Borne, High-Altitude Gravimetry (over)		62101F	7600	06	10
12. PERSONAL AUTHOR(S) Andrew R. Lazarewicz, Brenda J. Schilinski, Ralph J. Cowie, Catherine L. Rice, Peter Moss*, Leonard N. Carter**					
13a. TYPE OF REPORT Scientific. Interim.	13b. TIME COVERED FROM 11/82 TO 12/85	14. DATE OF REPORT (Yr., Mo., Day) 1985 December 31	15. PAGE COUNT 86		
16. SUPPLEMENTARY NOTATION *Bedford Research Associates **Air Force Reserves					
17. COSATI CODES			18. SUBJECT TERMS (Continue on reverse if necessary and identify by block number)		
FIELD	GROUP	SUB GR.	Balloon, Gravity, Gravimetry, High-Altitude		
19. ABSTRACT (Continue on reverse if necessary and identify by block number)					
<p>Gravimetry measurements from a high-altitude balloon were made in late September to verify global and upward-continued gravity models. The first flight was intended to provide balloon motion and environment data with a preliminary estimate of the quality of measured gravity values.</p> <p>A balloon operates in a dynamic, largely unpredictable environment; thus, the gravimeter senses accelerations due to balloon motions as well as gravitational acceleration. Independent measurements of balloon motions from an inertial navigation package (three accelerometers, three rate gyros, three-axis magnetometer and two tiltmeters) combined with ground tracking (X, Y and Z position and velocity) will allow for separation of balloon-induced accelerations from gravitational acceleration to 1 mGal, using tracking data to an accuracy of about 5 cm/sec in velocity for Eotvos corrections, and position to 1 m. → (over)</p>					
20. DISTRIBUTION/AVAILABILITY OF ABSTRACT		21. ABSTRACT SECURITY CLASSIFICATION			
UNCLASSIFIED/UNLIMITED <input checked="" type="checkbox"/> SAME AS RPT <input checked="" type="checkbox"/> DTIC USERS <input type="checkbox"/>		Unclassified			
22a. NAME OF RESPONSIBLE INDIVIDUAL ANDREW R. LAZAREWICZ		22b. TELEPHONE NUMBER (Include Area Code) (617) 377-5255	22c. OFFICE SYMBOL AFGL/LWG		

DD FORM 1473, 83 APR

EDITION OF 1 JAN 73 IS OBSOLETE

Unclassified

SECURITY CLASSIFICATION OF THIS PAGE

(mGal)

Unclassified

SECURITY CLASSIFICATION OF THIS PAGE

19. ABSTRACT - Continued

This first engineering flight was planned to coincide with the lowest seasonal wind velocities over Holloman Air Force Base, where AFGL has its permanent balloon launch facility. Mild wind velocities are desired to provide the most benign environment possible during the testing phase, and to keep the balloon within tracking range.

The experiment design, launch, and flight operations, and a first look at the data are presented.

11. TITLE - Continued

The Flight of DUCKY Ia (11 October 1983)

Unclassified

SECURITY CLASSIFICATION OF THIS PAGE

## Preface

The Air Force Geophysics Laboratory initiated the balloon-borne, high-altitude, gravimetry experiment to satisfy a Department of Defense (DoD) requirement. DoD's Defense Mapping Agency develops the gravitational model used with strategic missile systems. It is important to verify the accuracy of this model at various altitudes, particularly near missile launch sites.

We want to thank the Defense Mapping Agency gravity personnel and Ohio State University for supplying gravity models, the University of Toronto Institute for Aerospace Studies personnel for providing test and information for Section 2.3.2, the entire ground crew who made the balloon flight possible, Woods Hole Oceanographic Institute personnel for their support and information for Section 2.3.1, and summer students Brad Shultz and Suzanne Newfield.

Most of all, we want to thank Dr. Donald H. Eckhardt, Director, Earth Sciences Division, and Dr. Thomas P. Rooney, Chief, Geodesy and Gravity Branch, for their unrelenting patience and guidance with this project and report.



Accession For	
NTIS CRA&I	<input checked="" type="checkbox"/>
DTIC TAB	<input type="checkbox"/>
Unannounced	<input type="checkbox"/>
Justification .....	
By .....	
Distribution /	
Availability Codes	
Dist	Avail and/or Special
A-1	

## Contents

1. INTRODUCTION	1
2. EXPERIMENTAL DESIGN	7
2.1 Gondola Design Concept	7
2.2 Flight-Control and Data Systems	8
2.3 Sensors	9
2.3.1 Vibrating String Accelerometer (VSA)	9
2.3.1.1 Mechanical Layout of System	10
2.3.1.2 VSA System Description	10
2.3.1.3 Method for Frequency Counting	15
2.3.1.4 Discussion	16
2.3.2 University of Toronto Institute for Aerospace Studies (UTIAS) Instrument Package	16
2.3.2.1 Instruments	17
2.3.2.2 System Description	17
2.3.2.3 Calibration	18
3. FLIGHT OPERATIONS	19
3.1 Preflight	19
3.2 Flight History	20
4. DATA ANALYSIS	21
4.1 Objectives	21
4.2 Prediction Filter to Fill in Gaps of Radar-Tracking Data	30
4.2.1 Introduction	30
4.2.2 Linear Prediction Algorithm	30
4.2.3 Implementation Issues	31
4.3 Kalman Filter Model for Smoothed Estimates of Balloon Position	32
4.3.1 Kalman Filter Model	32
4.3.2 Data Used and Parameter Selection	37
4.3.3 Results	40

## Contents (contd)

4.4	Recursive Estimation Approach to Signal Analysis	40
4.5	Rotation	48
4.5.1	Introduction	48
4.5.2	Instruments and Methods	48
4.5.3	Summary	57
5.	CONCLUSIONS	61
5.1	Summary	61
	REFERENCES	63
	LIST OF ACRONYMS	65
	APPENDIX A: Relative Gravity Measurements at Holloman AFB, NM	67
	APPENDIX B: PCM/FM Telemetry Data	69
	APPENDIX C: Gravity Payload Preflight Schedule	75
	APPENDIX D: Control Center Log	77

## Illustrations

1.1	A Sketch of the Balloon Gravity Concept	3
1.2.	A Sketch Showing Exaggerated Motions of the Instrument Package	4
1.3.	The Ground-Tracking System Consists of Three Ground Radar Stations Yielding Range and Azimuth	5
1.4.	Typical Winds Over Holloman Air Force Base are Shown	6
2.1	VSA System Block Diagram	11
2.2	A Sketch of the VSA Sensor	12
3.1	A Photograph of the Payload, Named DUCKY Ia, Just After Transport to the Launch Site	22
3.2	A Photograph of the Payload, Tested and Ready for Flight, at the Launch Site	23
3.3	A View of the Balloon Inflation With DUCKY Ia in the Background	24
3.4	A Photograph of DUCKY Ia Minutes After Launch	25
3.5	A Plot of the Flight Path of DUCKY Ia	26
4.1	A Comparison of Flight Altitude and Gravimeter Measurements for the Entire Flight	28
4.2	A Comparison of Flight Altitude and Gravimeter Measurements for Flight Altitude Only	29

## Illustrations (contd)

4.3	Example of a Gap of Eight Points in WSMR Tracking Data	33
4.4	Example of Section of Data With Two Gaps, Each of Length 6	33
4.5	Example of Section of Data With Two Gaps, Each of Length 6	35
4.6	Block Diagram of Kalman Filter Used to Smooth Tracking Data Using the Flight Inertial System	38
4.7	Plots of the Detrended Altitude and Vertical Acceleration for the Period of 1730 - 1807 Zulu	39
4.8	Comparison of Raw Radar Altitude Data With the Kalman Filter Output	41
4.9	Comparison of Vertical Accelerations Sensed by the Flight Inertial System With the Kalman Filter Estimate	42
4.10	Comparison of Vertical Velocity Sensed by the Flight Inertial System With the Kalman Filter Estimate	43
4.11	A Plot Showing Measured Gravimeter Error Due to Pendulum Swing	50
4.12	Example of Raw 3-Axis Accelerometer Error in Cartesian and Spherical Coordinates	51
4.13	Example of Smoothed 3-Axis Accelerometer Error in Cartesian and Spherical Coordinates	52
4.14	Example of Raw 3-Axis Rate Gyro Data and Detrended Version	54
4.15	Example of Smoothed 3-Axis Rate Gyro Data and Detrended Version	55
4.16	Comparison of Raw Compass Data (to Magnetic North) With Raw Magnetometer Estimate of Compass Angle (to True North)	56
4.17	Magnetometer Data Minus NASA Magnetic Field Model in Spherical Coordinates	58
4.18	Absolute Angle About Z-Axis as Measured by (Top to Bottom) Compass, Magnetometer, and Integrated Z-Gyro (With Arbitrary Zero)	59
4.19	Differences Among Measurements Shown in Figure 4.18	60

## Table

1.	Results From 10 Consecutive 10-sec Segments.	46
----	--	----



Balloon-Borne, High-Altitude Gravimetry  
The Flight Of DUCKY Ia  
(11 October 1983)

1. INTRODUCTION

Gravity field values at high altitudes, between altitudes for aerial surveys and satellite orbits, (e.g., 30 km), are normally estimated from upward continuation of surface measurements, downward continuation of satellite measurements as computed from orbital perturbations, and/or geoid models. These techniques are well-developed with generally accepted results, but are subject to some limitations. Upward continuation depends upon the quality and distribution of surface data, usually nonuniformly spaced, and taken from different surveys; thus, gaps and uneven spatial distribution may result in inaccurately upward continued estimates. With increasing altitude, short wavelength information on crustal structure is attenuated, not recoverable from downward continuation from satellite altitudes. Geoid models tend to emphasize wavelengths longer than about 30 km, and are well-known only over oceanic areas.

Verifying gravity data bases and models requires establishing the validity of the models at locations where measurements have not been made. While such models currently can be tested effectively at ground level, their validation at altitude awaits the development of a suitable approach. The Air Force Geophysics Laboratory (AFGL) is developing a program to verify gravity model estimates by

---

(Received for publication 31 December 1985)

measuring gravity directly using high-altitude balloons. The basic concept is shown in Figure 1.1. A gravimeter package suspended beneath a balloon is in a dynamic and largely unpredictable environment, sensing not only the gravitational acceleration of the earth but also all accelerations due to the motions of the balloon system. An exaggerated sketch of kinematic balloon motion is shown in Figure 1.2. For a specified time interval (e.g., 1 second) during which a measurement is made, the variation in balloon accelerations is expected to be significantly greater than the variation expected in the Earth's field. Therefore, additional instrumentation is required to measure as many balloon motions as possible, such as rotation, bobbing, and swaying. As all such ancillary sensors are dependent on the local inertial frame, gravitational acceleration cannot be separated from vertical balloon accelerations without additional data acquired independently of the balloon's reference frame. These independent data are extracted from balloon tracking (Figure 1.3) which must accomplish three objectives: 1) the measurement of the gravimeter package accelerations (especially the vertical) referred to a ground-based coordinate system; 2) the measurement of velocity for estimation of the Eotvos effect; and 3) the measurement of the gravimeter position, which is used as an input to the gravity model. Combining balloon data with tracking data allows the separation of balloon-induced accelerations from gravitational accelerations.

The long-term goal is to determine gravity to 1 mGal ( $10^{-3}$  cm/sec<sup>2</sup>), and in support, obtain instrument motion data (worst-case limits) of accelerations to 1 mGal, velocity to 5 cm/sec, and position to 3 m in all three orthogonal coordinates.

The balloon launch was set to coincide with the lowest seasonal wind velocities (Figure 1.4) over Holloman Air Force Base where AFGL has its permanent balloon-launch facility. The mild wind velocities are desired to provide the most benign environment possible during the testing phase so that the analysis effort may focus on the performance of the gravimeter system. Balloons have been flown up to 150,000 ft where the air pressure is less than 1 mm of Hg. Temperatures can range from -70° C at night to almost 40° C on exposed parts of the gondola's aluminum framework in the daytime. The instrument packages had to withstand the shock and vibration associated with both launch and landing. Even with a parachute and a crush pad on the gondola, accelerations up to 8 g may be expected on landing. Ideally, the instrument packages would be self-contained except for telemetry and batteries.

The instruments were also operated in a strepdown mode; i.e., the instrument axes are not fixed with respect to inertial space but are attached to the instrument package itself. Since the packages are rigidly fastened to the balloon gondola, the instrument axes correspond to a local coordinate system in the gondola.

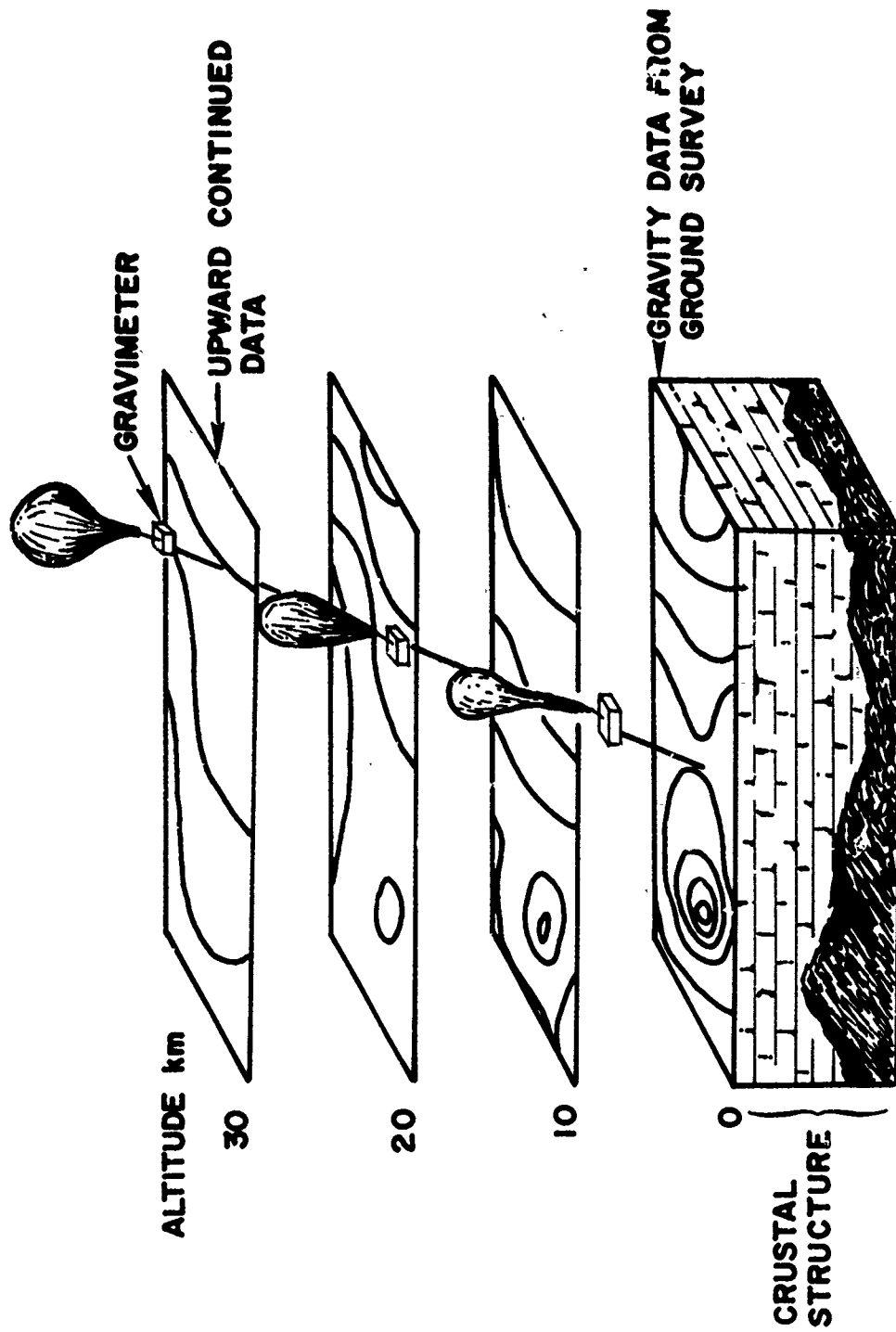


Figure 1.1 A Sketch of the Balloon Gravity Concept. Gravity data is upward continued from the surface, and tested at altitude from a balloon-borne platform

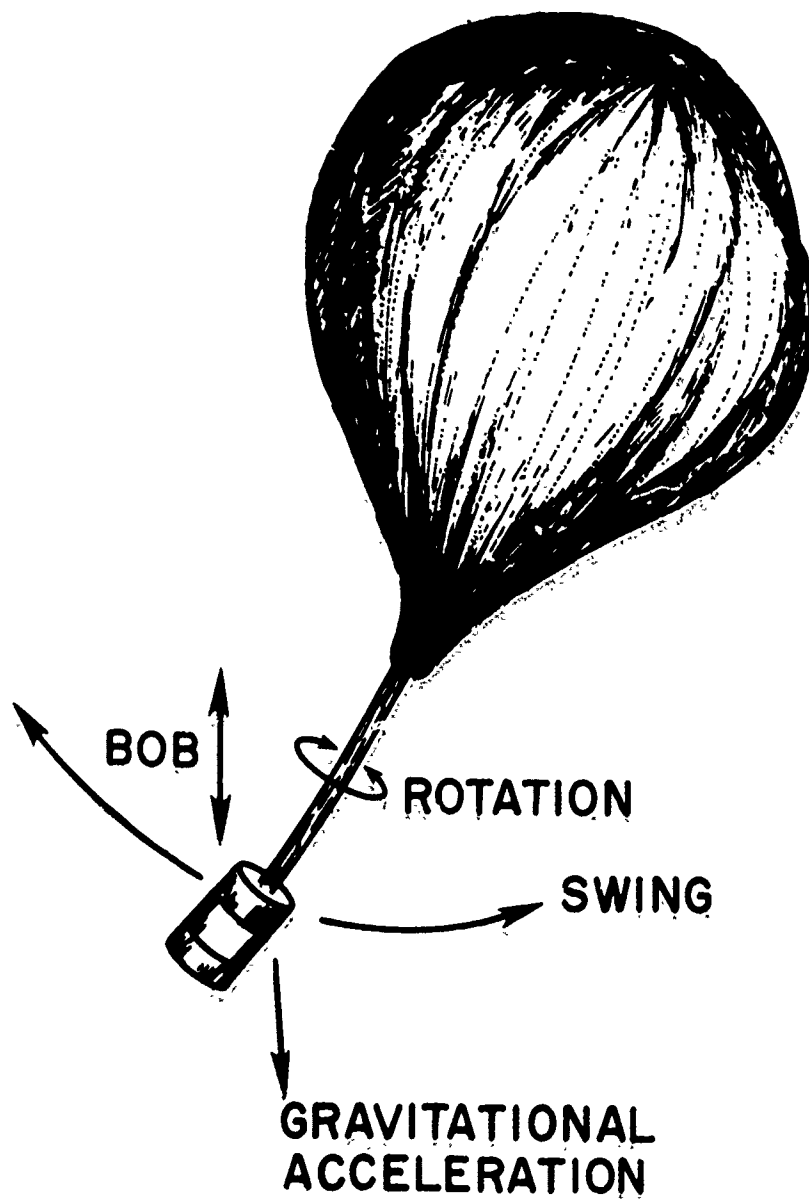


Figure 1.2 A Sketch Showing Exaggerated Motions of the Instrument Package. Each of these motions contributes to a vertical acceleration term; thus, confusing the gravimeter data

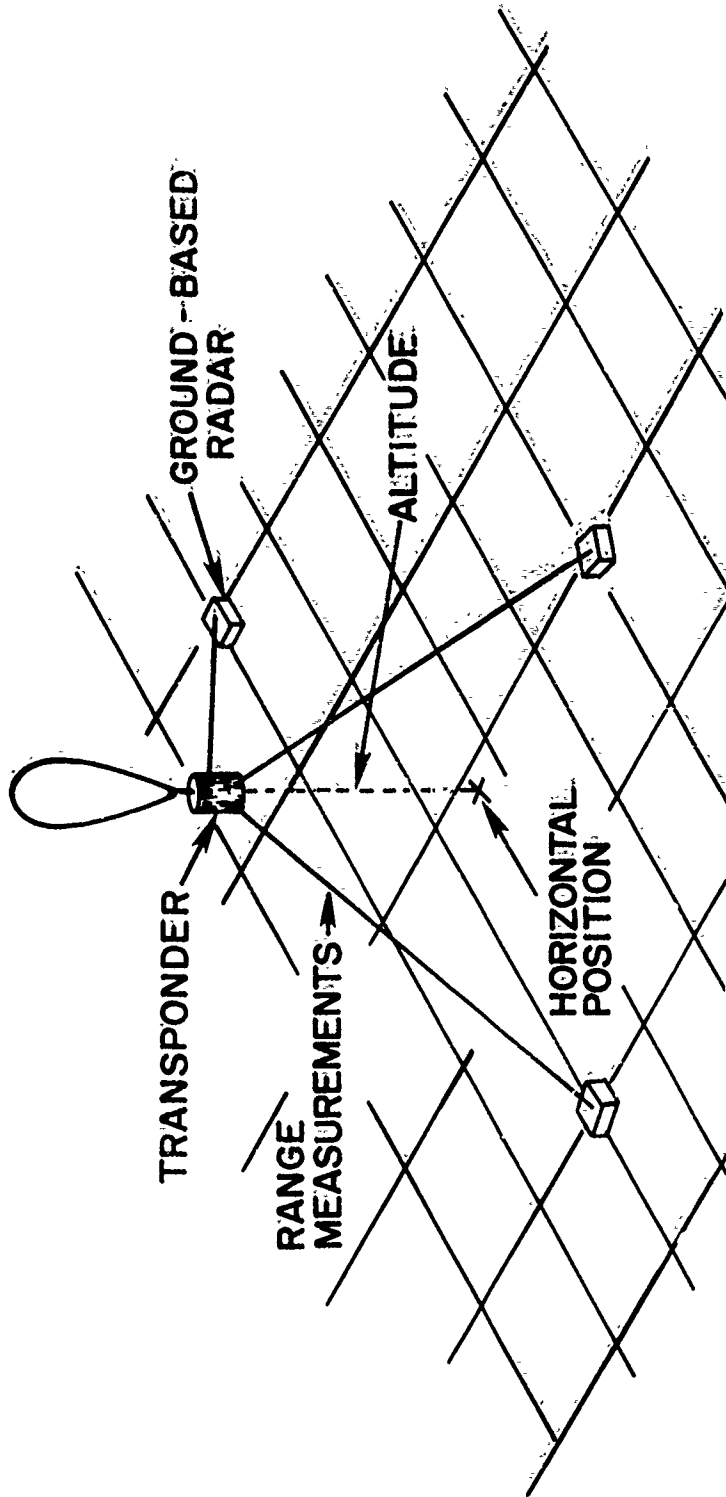


Figure 1.3 The Ground-Tracking System Consists of Three Ground Radar Stations Yielding Range and Azimuth.

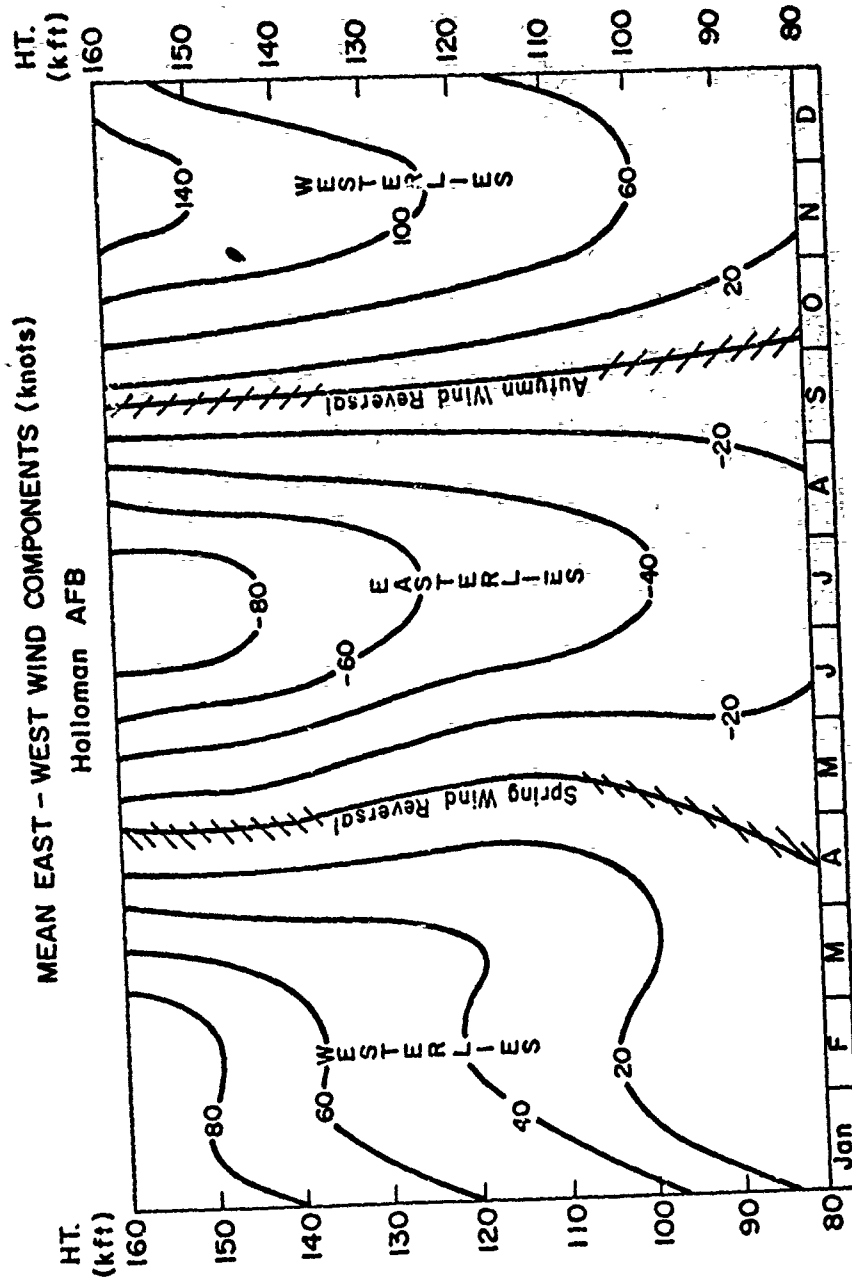


Figure 1.4 Typical Winds Over Holloman Air Force Base are Shown. To minimize balloon and gondola motion, flights are planned to occur during the seasonal wind reversals

## 2. EXPERIMENTAL DESIGN

### 2.1 Gondola Design Concept

General requirements for a gravity measurement flight system began to develop in March 1983. A target flight data for the completed system was set for October 1983. This relatively short lead time appeared reasonable because development of a balloon-borne motions-sensor package had already been started under an AFGL contract with the University of Toronto. This package would contain accelerometers and strapdown rate gyros aligned in three orthogonal axes for determining altitude and motions of the payload.

The scientific goal was to resolve accelerations in the X, Y, and Z planes to one part in  $10^7$ . This meant every effort had to be made to minimize extraneous motion and to attempt to achieve a payload configuration that would hang beneath the balloon as close to vertical as possible. In essence, we should try to produce a true plumb bob when airborne. We also selected a symmetrical shape to reduce the effect of wind and turbulence.

Attachments were designed to limit the tendency of a lengthy flight train (balloon-recovery parachute and gondola) to wind up and unwind as the system ascends to float altitude. During ascent, the balloon changes shape as it rises and imparts rotation to the system, storing this rotational energy in the in-line, elastic nylon recovery parachute. The mechanical aspects of the flight-system design thus became paramount considerations to minimize undue linear motions and rotation. Essentially, we limited the degrees of freedom in the rigging, and designed for maintenance of balance and verticality during operation of any on-board control devices such as ballast dispensing and valving off helium lifting gas.

Soon other mechanical problems surfaced, due to the need to physically and electrically integrate the tracking beacons, the radar transponder, the recovery beacon, the two down-link data transmitters, the six antennas, and a full-time command-control capability, and to provide internal and external power system compatibility. Temperature controls for the prime sensing devices were required to minimize drift and subsequent error in measurement.

The melding of several independent, though closely interrelated, subsystems necessitated devising a gondola system that could provide sectional disassembly and operational independence for service and individual testing/calibration, yet permit flexibility for modification. The size and form factor of the gondola was also limited by the launching method to be employed for the balloon system. A dynamic launch method, with the gondola suspended from the boom of a mobile P&H 30-ton

crane, limited the vertical size that could be handled safely. Using a balloon of 2.9 million cubic-foot volume, the payload weight had to remain under 2,500 lbs including 445 lbs of pourable glass-bead ballast, in order to reach the desired float altitude and achieve the desired flight profile of two sampling altitudes.

The most suitable shape for meeting all requirements was a long cylinder that consisted of five sections bolted together on internal flanges. All sections were 34 in. in diameter. Section heights varied from 23.5 in. to 33 in. for a total stacked height of 11 ft 3 in. A four-point suspension, using all-stainless cable (wire rope) with adjustable, fine thread turnbuckles in each leg, terminated into a singlepoint fixture for attachment to the launch crane's tri-plate release device.

The parachute was specifically oversized to slow the impact velocity to 15 to 20 ft/sec, and a crush pad of stepped, corrugated cardboard 16 in. thick was attached at the base of the cylindrical gondola. A roll bar (impact-absorbing crush ring) 7 ft in diameter, concentric with the cylinder axis, assured that with anticipated horizontal velocities of 30 to 50 ft/sec, the gondola would lie over safely with minimal physical damage upon ground impact. The base of the crush pad carried impact switches designed to release one set of parachute suspension-harness risers to collapse the chute and prevent the possibility of dragging the payload across the ground after impact.

The exterior of the cylindrical gondola was skinned with aluminum. When flight-ready, it was wrapped with 2-in. thick fiberglass "Certainteed" pipe insulation, with an All Service Jacket (ASJ) vapor barrier of aluminum foil, and glass-reinforced, whitecoated Kraft laminate, which served as a reflective, white outer surface, finished with superior compression resistance for added protection.

## 2.2 Flight-Control and Data Systems

The design of the flight-control system followed standard AFGL practice of providing primary and backup systems to ensure positive experiment control and redundant flight-safety control via separate power systems. In this case, because of the stacked sectional design of the gondola, the independent primary and backup systems were located in the same gondola section. One section was to contain all necessary battery power. This was achieved by using two "freeze-pack" thermal containers, each housing fourteen 80 Ah BB622/U batteries, configured in such a fashion as to provide isolated power sources for the various instruments and sensors aboard the gondola.

There were five separate internal power sources, plus one with the capability of continuous external power. The power system weighed approximately 322 lbs.



Each power source could be powered up or down by radio command of either the primary or backup digital command systems.

A single instrument frame, 17 x 17 x 10½ in., housed all flight-control electronics, two digital command units, housekeeping sensors and monitors, power control interface units, and one PCM (pulse-code modulation) data encoder. This instrument frame was housed in a laboratory-grade, low-temperature-insulated container (bio specimen "freeze-pack") for environmental protection and temperature control. This method of packaging permits very high flexibility as the final system configuration is composed of an assembly of modular items, all interconnected by a master harness terminated in a master patch-panel-type connector interface for inputs and outputs.

The gondola had two telemetry down links and two radio-command up links. Both telemetry links were continuous, and employed standard IRIG (Inter Range Instrumentation Group) PCM/FM data format. The housekeeping and motion-sensing data were sampled at 128 kilobits per second, using ten bits per word, most significant bit sent first; there were 47 analog words (channels), and three digital words with two synchronizing words without parity check, included per data frame. The output code was transmitted Bi-Phase FM on a 500 kHz modulated, 2.2 GHz carrier with 2 w RF output.

The science data from the Vibrating String Accelerometer (the prime gravity sensor), with its own housekeeping and monitoring information, was transmitted on a separate 2.2 GHz PCM channel due to the nature of the sensor output and sampling rate desired. For this we utilized a 19.2 kilobaud bi-phase encoder of 30 words per frame (27 analog and 3 digital). This was also a standard IRIG format, 10 bits per word.

On the ground, both data streams were recorded on wideband FM analog tape, and simultaneously stripped out for display in real time, on digital meters or graphic chart recorders. Thirty-six strip chart data channels were displayed in real time during the flight to assess program progress. A complete listing of the data channel assignments appears in Appendix B.

## 2.3 Sensors

### 2.3.1 VIBRATING STRING ACCELEROMETER (VSA)

The Vibrating String Accelerometer (VSA)<sup>1</sup> is a single-axis accelerometer originally designed for the Atlas missile navigation system in the 1960s. When the VSA was deemed obsolete for the Atlas, the Woods Hole Oceanographic Institution

---

1. Bowin, Carl O., Scheer, Eddie, and Goldsborough, Rob (1984) Technical Report - Balloon Environmental Test Report, AFGL Contractor Report.

(WHOI), Woods Hole, MA acquired a collection of VSAs from government surplus stock. WHOI developed and built a shipborne gravimeter system based on the VSA,<sup>2,3,4</sup> and successfully used it in geophysical research over the subsequent years. When the balloon-gravity program came into being, WHOI proposed to build a gravimeter/inertial system for AFGL. In March 1983, WHOI came under contract to AFGL and successfully built a gravimeter system in time for the planned September 1983 launch.

#### 2.3.1.1 Mechanical Layout of the System

Six basic modules were developed at WHOI and placed aboard the gondola: 1) The VSA and Oven System: a "can" (VSA two-stage oven) housing the VSA and its temperature-control components and circuitry; 2) The Processing System: a cardcage holding six circuit cards; 3) The Oscillator: a shielded "cube" holding two more cards: a 10 MHz crystal oscillator and associated oscillator control circuitry; 4) The Encoder: (obtained from AFGL) that relayed acquired VSA data to ground; 5) The Heat Sink: a large heat sink upon which were mounted both a power supply that converted power from the AFGL batteries for use in VSA circuitry, and a set of power transistors used to drive VSA heater blankets; and 6) The Front Panel: used for monitoring and adjusting VSA components while the system was on the ground.

In addition, a Micromation microcomputer, a Kennedy tape drive, an eight-digit display, and assorted power supplies and test equipment were supplied by WHOI for testing, and for acquisition of data taken on the ground prior to the experiment.

#### 2.3.1.2 VSA System Description

Figure 2.1 is a block diagram schematically illustrating the basic components and interconnections amongst the VSA system components.

##### VSA and Oven System

The principal components of the can are: 1) VSA Sensor: The VSA is a device consisting of a mass suspended by two metal bands (strings) under tension (Figure 2.2). The tension on, and the length of, each string is set so the resonant frequency is about 4 kHz at a very high Q (value not available). Due to the high Q, the strings will oscillate (at resonance) very easily, and ambient noise

2. Bowin, Carl, Wing, Charles G., and Aldrich, Thomas C. (1969) Test of the MIT vibrating string gravimeter, J. Geophys. Res. 74, 12:3278-3280.
3. Bowin, Carl O., Folinsbee, Allin, and Aldrich, Thomas C. (1970) Test of digital VSA sea gravity meter and comparison with LaCoste and Romberg gyrostabilized gravity meter (Abstract), Trans. Am. Geophys. Union 51, 4:261.
4. Bowin, C., Aldrich, T. C., and Folinsbee, B. A. (1972) VSA gravity meter system: tests and recent developments, J. Geophys. Res. 77:2018-2033.

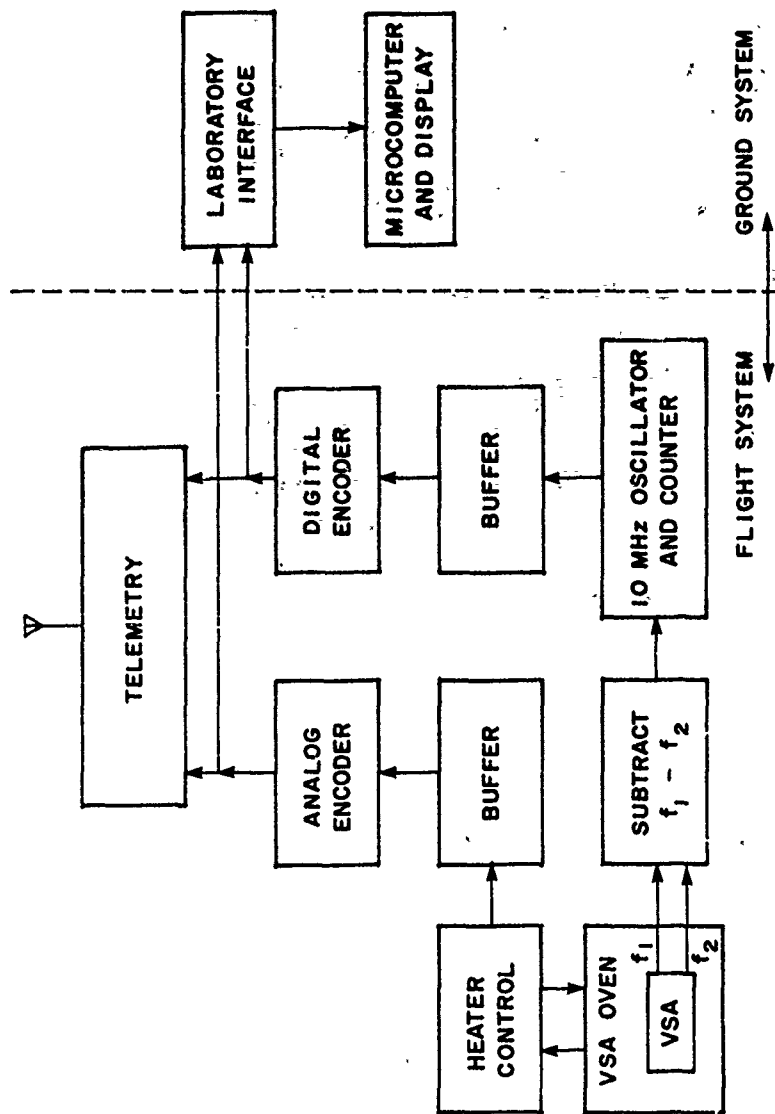


Figure 2.1 VSA System Block Diagram. The ground system is used only for development and testing

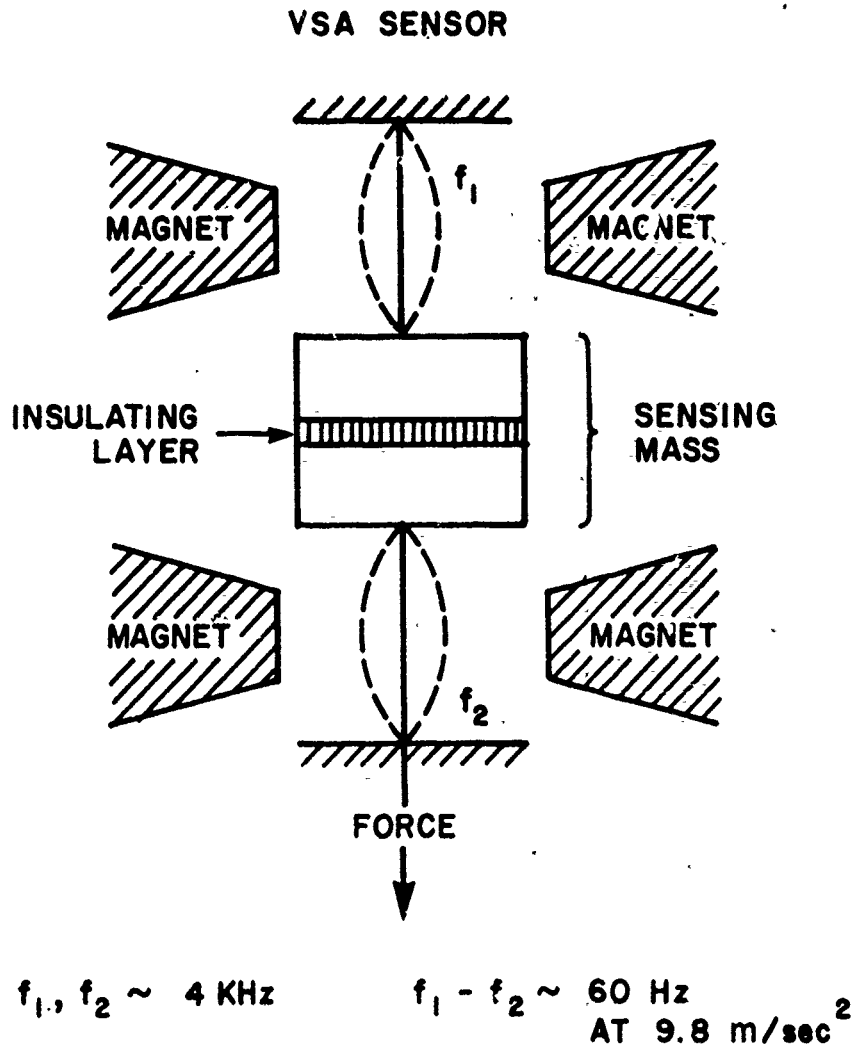


Figure 2.2 A Sketch of the VSA Sensor. Two strings under tension are separated by a mass. A force acting on the mass along with the strings will cause different tensions on each string; thus, each string will have a different resonant frequency. The VSA system measures the acceleration from the beat frequency of the two strings. The resonant frequency of each string is about 4 kHz; the beat frequency at 1 g is about 60 Hz

is enough to drive the oscillations. The surrounding magnets sustain the oscillations. The oscillation creates an electromagnetic force (EMF) due to the ambient magnetic field. The EMF is sensed, amplified, and fed back to the strings. When an acceleration is sensed in the sensitive axis (along the strings), the force acting on the mass results in different tensions acting on the two strings. The string in the direction of the acceleration is at a lower tension than the opposite string. At 1 g, the difference in resonant frequencies is about 60 to 64 Hz. Thus, when the two frequencies are mixed, three narrow bands of frequencies exist: 65 Hz, 4 kHz, and 8 kHz. When low-pass filtered, the final VSA output frequency is about 65 Hz, and it is this frequency that is a measure of the along-axis acceleration. For this flight, we chose to sample the VSA output every 10 cycles, giving an effective sampling rate of about 6.5 Hz. The circuitry was designed to yield either a frequency count or the period, the latter being the choice for the flight.

2) Osc/Amp: An Oscillator/Amplifier circuit that effectively sustains oscillations in one of the two strings of the sensor by positive feedback. The output of the circuit is a sinusoidal signal with a nominal frequency of 4.5 kHz. There are two of these circuits in the can, and two strings in the sensor. The difference in the frequency of the two resulting signals is directly proportional to the acceleration and/or the component of gravity experienced along the input axis of the sensor:  $a = K * f_d + B$ , where  $a$  is acceleration in milligals,  $K$  is the scale factor,  $f_d$  is the difference frequency in Hz, and  $B$  is a bias term in milligals. Prior to the experiment, a scale factor determination was performed, and the following values obtained:

$$K = 15218.29659 \text{ (milligals/Hz)} \quad (2.1)$$

$$B = 4980.720047 \text{ (milligals)} \quad (2.2)$$

A rough value for  $f_d$  at 1 G acceleration is 64.1 Hz. 3) Inner and Outer Ovens: A two-stage oven is used to maintain the temperature of the sensor; the "outer" housing the "inner." Each oven contains two thermistors that sense temperature within the controlled volume: a "monitor" thermistor that is used solely for temperature observation, and a "control" thermistor that is connected in a bridge configuration with high-quality resistors and connected to a preamp mounted in the can. This circuitry is used for controlling the temperature by regulating the power supplied to heating blankets mounted around each oven.

#### VSA Processing System

Six circuit cards were mounted in a cardcage and they functioned as follows:

1) Heater Amp Card: The outputs from both inner and outer can thermistors and their associated preamps in the can are scaled and amplified on this card and then

are sent to the power transistors on the heat sink which control the power sent to the heater blankets around the ovens. At an intermediate point in the signal routing on this card, control-voltage signals are also output to jacks on the front panel for testing and monitoring purposes. 2) Monitor Amp Card: Two bridge/amplifier configurations are found on this card. These are connected to the inner and outer monitor thermistors. The outputs are sent to front-panel jacks and to the encoder (via the analog buffer card). Two more amplifiers are also included for measurement of the resistances of two other thermistors: one mounted on the heat sink, and the second on the mounting plate of the VSA oven. These are intended for the observation of ambient temperature within the gondola. The output of this pair of amplifiers is sent to the analog buffer card where, like the monitor signals, it is unaltered and passed directly to the encoder. 3) Subtract Card: This board effectively performs the "subtraction" of the frequencies of the two sinusoidal outputs of the can. One output is a square-wave signal with a frequency of  $f_d$  used in the Phase Lock Loop (PLL) board in the cube. A second output, another square wave with frequency  $f_d/N$ , where N can be selected to be either 10 or 100 with an on-board switch, is applied to the cube's Period Counter (PC) circuit. 4) Analog Buffer Card: Two signals from the Heater Amp card, the inner and outer control voltages are scaled on this board and buffered for output to the analog section of the encoder. Likewise, the actual voltages on the inner and outer heater blankets are scaled and buffered along with the raw battery voltage. Finally, four signals from the Monitor Amp card, heat sink temperature mounting plate temperature, inner monitor temperature, and outer monitor temperature pass undisturbed through this card on their way to the analog inputs of the encoder. 5) Digital Buffer Card: Thirty-two digital input lines (bits) from the cube are buffered on this card, and 30 of them are output to the digital word inputs of the encoder. Only the 30 Least Significant Bits (LSBs) out of 32 bits are sent due to the limitations of the telemetry; the remaining two bits are recovered in post-flight processing. 6) Display/CPU Buffer Card: The same 32 digital input lines as above are also input to this card, which multiplexes them in two separate ways for: a) the display device, and b) the microcomputer. Both outputs include an 8-bit data word, and associated address lines. This card is used only for on-the-ground testing and measurement.

#### Oscillator

The shielded "cube" contains two circuit boards and a high-precision 10 MHz oscillator. The use of a separate, shielded container for the high-frequency parts of the system was intended to minimize possible noise problems. The oscillator is mounted on a motherboard upon which is emplaced both an oscillator oven control

circuit and a set of two connectors that hold the PLL and PC cards. The PLL and PC circuits operate concurrently. The purpose of both is the high-resolution determination of  $f_d$ . The outputs of both (32 digital signals) are brought out to two Blue Ribbon connectors on the cube. The pinout of both connectors is the same, so that the selection of the PLL or PC mode of operation requires only connection of the data cable (between the cardcage and the cube) to the desired connector. The PC mode of operation was used for the flight. A discussion of the differences between the PC and PLL methods appears below, in the section on individual card schematics.

#### Encoder

The encoder is an AFGL-provided device that will accept three 10-bit digital words and 59 0-5 VDC analog signals. These are multiplexed into one telemetry stream for transmission.

#### Heat Sink

The heat budget of the gondola is not a simple issue. Due to the lack of atmosphere at altitude, convection does not remove heat from the gondola. Virtually all the heat must be removed by radiation, and the gondola system achieves equilibrium at a temperature above that at 1 A. The heat sink is designed to conduct heat out of the VSA and move it to the gondola frame.

#### Front Panel

The front panel is simply a switch and connection panel for ground testing, and is completely disconnected during flight.

### 2.3.1.3 Method for Frequency Counting

Since the value of  $f_d$  at 1 g is roughly 64.1 Hz, the PLL chip outputs a square wave of 256 kHz mean frequency. By its very nature, the frequency counting technique averages the desired information over the gate time, but also performs some analog filtering of the data. This technique provides a convenient, fairly high resolution representation of the average frequency of  $f_d$ , with the disadvantages of observation of  $f_d$  through a "fuzzy" window caused by the nonlinearities in the analog filtering of the PLL, and the phase-detector stages of the chip. In order to provide a less processed data set for the balloon experiment, the period counting method was actually used.

At certain times, however, it was advantageous to use the frequency counting data for on-the-ground testing, since a direct display of the accelerations experienced by the sensor ( $4096 * f_d$ ) was available in real time.

In period counting, as in frequency counting, frequency variations of  $f_d$  are averaged over the time between N zero crossings. N was 10 during the actual

flight, so that averaging time at 1 g acceleration was  $10 \cdot (1/64.1)$  or roughly 156 msec. Less filtering would have been accomplished for  $N=1$ , but then the data rate would have been too high for the acquisition system. With this method, no other filtering was done, so a "purer" form of acceleration data was recorded. One drawback of this approach is the fact that data were sampled at irregular intervals. An interpolation scheme using bilinear interpolation was used in order to produce a constantly sampled data stream amenable to further processing techniques.

#### 2.3.1.4 Discussion

Of the 230,000 points collected during the balloon experiment, only 64 "glitches" could be detected in the data. Some of these errors were attributable to telemetry dropouts, but some errors occurred in the WHOI circuitry, in particular the latching circuitry implemented in the PC counter. Special care was taken in this circuitry to ensure that latching would not occur during clock transitions. It would, perhaps, be worthwhile to look at the circuits again to see if any improvements can be made. Nevertheless, considering the environment, an error rate of 64/250000 is acceptable.

The IC logic type used throughout was high-speed CMOS (HC) which, with its low power consumption and higher fan out, seemed to work very well. The only problem encountered occurred in the interface between this type of logic and other more standard types. For instance, before the flight, there was a flurry of activity resulting from a failure of a few of the WHOI chips. These chips were of the HC type, and were located at the interfaces between the gravity system and the encoder, the test computer, and the display. The latter components all used the more standard low power Schottky TTL. It would be wise, when redesigning this system, to keep the HC logic, but to pay more attention to interfaces with other logic types.

#### 2.3.2 UNIVERSITY OF TORONTO INSTITUTE FOR AEROSPACE STUDIES (UTIAS) INSTRUMENT PACKAGE

The UTIAS flight-test package<sup>5</sup> consisted of three rate gyros and three accelerometers. The rate gyros were mounted with their axes orthogonal to each other, and would measure the pendulation and rotation rates with respect to a set of axes fixed to the instrument package. Relative angular displacements would be

---

5. DeLeeuw, J. H., and Kung, W. L. (1984) Development of motion-sensing package for high-altitude balloons, University of Toronto Institute for Aerospace Studies, Scientific report submitted under contract F19628-82-C-0041.



obtained by integrating the gyro rates. The vertically mounted accelerometer would sense the balloon's vertical acceleration superimposed on the earth's gravitational field. After removing the gravity signal from the measurements, they could be integrated twice to yield relative vertical displacements. A three-axis magnetometer that detects the components of the earth's magnetic field about three orthogonal axes was also included in the balloon motion-sensing package.

#### 2.3.2.1 Instruments

Rate Gyros: The rate gyros are GG440 A7 GNAT miniature rate gyros made by Honeywell. A torsion bar spring is used to provide a restoring torque about the gyro's precessional axis so that the precession rate is proportional to the input rate. The rate of precession is detected and converted to an electrical signal by the signal generator/pickoff. Two rate gyros, designated X and Y, were assigned to detect balloon pendulation. The other rate gyro, called the Z-gyro, was used to measure the balloon's vertical rotation. The rate gyros required 400 Hz excitation, which was provided by an Abbott power supply. The output of the signal generator must be demodulated to obtain a signal proportional to input rate.

Accelerometers: The vertically mounted or Z-accelerometer should be able to sense the up-and-down motion of the balloon system. Assuming sinusoidal motion, the maximum accelerations involved are a few hundredths of one g. The accelerometers are Sundstrand QA1100s. These instruments are force-feedback acceleration transducers that feature a completely elastic seismic suspension, made from amorphous quartz, that virtually eliminates bearing friction. The servo electronics are completely contained within the instrument, which also has a convenient self-test capability. The output voltage signal is developed across an internal load resistor.

Magnetometer: The three-axis magnetometer is a Schonstedt SAM-73C. It is a sensitive instrument and exhibits highly linear response on all axes. Its main purpose is to provide an absolute azimuth reference from measurements of the horizontal components of the earth's magnetic field.

#### 2.3.2.2 System Description

The motion-sensing package hardware is housed in a pressure-tight aluminum enclosure. Adjustable pads on each corner and the two bubble levels enable the package to be leveled after mounting. The enclosure consists of a baseplate and a cover, with an O-ring providing the seal between them. There is a port on the cover that allows the package to be vacuum-tested. A pressure-tight container was necessary because the accelerometers were not hermetically sealed. This meant that changes in air pressure could affect the instrument's internal damping and, hence, its performance.

The accelerometers are housed in a triaxial mounting block of anodized aluminum that is fastened to a Lexan base. This base can be leveled independently of the aluminum baseplate. The arrangement for the rate gyros is similar. These sensors are surrounded on five sides by blue styrofoam walls that, with the Lexan plates, form an insulated compartment. The enclosure is heated to a constant temperature of 50° C to prevent external temperature fluctuations from affecting performance. The "oven" is heated by a Darlington power transistor regulated by an on/off control circuitry. Two sensors provide a readout of the "oven" temperature, and the temperature of the rest of the instrument package.

The problem of maintaining this "oven" at a constant temperature over several hours is complicated by the fact that the rate gyros themselves are generating heat. Eventually, if this excess heat is not removed, the temperature cannot be regulated, and the sensors might be destroyed. Calculations showed that the extra heat could be absorbed by the gondola environment if its temperature remained below a certain level. There was no guarantee of this being the case, however, and the problem was solved by attaching a heat sink for the motion-sensing package.

#### 2.3.2.3 Calibration

Magnetometers: No calibrations were performed for the three-axis magnetometer because of the lack of large Helmholtz coils. Instead, the manufacturer's calibration data were used to reduce the flight data.

Rate Gyros: The rate gyro calibrations were made using a Genisco Model C-181 rate table that is capable of rotating at rates from 0 to 1200 deg/sec in both clockwise and counterclockwise directions. The gyro to be calibrated had its sensitive axis aligned with the rotational axis of the rate table. This meant that a special mounting jig had to be used for testing the X- and Y-rate gyros. Power and signal lines were routed through slip rings on the rate table. The high- and low-sensitivity rate gyro outputs were measured using a Hewlett Packard true RMS meter. Readings were obtained as the rate was increased in steps from 0 to 1 deg/sec and then decreased for both clockwise and counterclockwise rotation.

Accelerometers: Static calibration of the accelerometers was performed by tilting the package along the sensitive axis of each sensor, and measuring the component of earth's gravity. The experimental setup was similar to that used previously at UTIAS for calibrating the flight-test package. The instrument package was fastened to its mounting jig, and the whole assembly was clamped to a large turntable that could be rotated about a horizontal axis. The sensor outputs were read out on a true RMS meter.

### 3. FLIGHT OPERATIONS

#### 3.1 Preflight

Approximately two weeks ahead of a scheduled launch date, all equipment and personnel are expected to arrive on location at Holloman AFB, New Mexico. Equipment is unpacked and inspected visually for damage. Individual modules are disassembled and checked for loose connections or components, then reassembled and tested for electrical performance following specific checklists. Calibrations are reverified as necessary to get the flight control integrated with the "science" in preparation for an "all-up" system checkout run. This usually consumes about three or four days during which time the final battery preparation, charging, and packaging are accomplished. After preliminary subsystem tests are completed, a full-scale, open-loop telemetry and radio command test is performed, and preliminary data tapes and chart records are run to verify the absence of undesirable interference (or presence of the same) that must be eliminated before proceeding on schedule.

After a series of acceptable preliminary test runs, the complete payload is taken to the Holloman environmental test facility for a temperature and pressure-controlled test run, lasting from four to six hours, to simulate a typical ascent, float, cold soak, and descent as would be encountered during a balloon flight. The chamber controllers attempt to follow the requested profile, and the opportunity to pause and make changes during runs permits corrective action if problems show up during the test. This is a full-scale, open-loop, data-taking, test run. Chamber testing continues until the complete system successfully passes the full six-hour profile.

After successful environmental tests are concluded, the final stages of flight preparation begin. This includes recharging batteries, refining checklists for prelaunch and flight-line activities, developing a specific timetable, schedule of events, and detailed contingency plan to circumvent potential anomalies should they occur during the launch or flight phases of the operation. Once schedules and corrective action plans are finalized, the detailed meteorological analyses of local surface weather, flight-path forecast, trajectory, and final impact predictions begin in earnest, with daily briefings aimed toward the commencement of a final countdown for launch.

A typical log of flight events (Appendices C and D) shows a highly labor-intensive effort encompassing 24 consecutive hours of solid activity, and involving a team effort of between 20 to 30 people to produce a 6- to 8-hour scientific balloon mission. The team effort involves planning, documentation, instrument

preparation, and testing. It involves ground support equipment, vehicle readiness, payload transport, convey roll-out, launch layout, and flight rigging at the launch site, as well as final prelaunch verification checkouts, balloon layout and inflation, launch ascent to float altitude, change of float altitude, if called for, and valve down and level off. Following the completion of the experiment, it is necessary to set up and accomplish flight termination.

The payload descent and recovery phase can be critical. When the scientific side of the mission is finished, the focus changes, and the control-center team concentrates on accurately predicting a safe and suitable impact point. They must also specify a location for descent penetration of flight level 440 (44,000 ft MSL) for transmittal to the FAA regional control center. By judicious use of available meteorological data, flight-control experience, and command/control of the balloon and payload, the balloon system is steered to the desired termination point where the payload is separated from the balloon by radio command. The balloon is thereby destroyed, the recovery parachute is deployed, and a prediction of parachute drift to the impact location is transmitted to the tracking aircraft and the FAA. A constant plot of altitude and position is maintained throughout flight, and all participants are in constant communication via several radio networks and telephone. The tracking aircraft maintains contact with the predeployed recovery mobile force which is equipped with suitable vehicles, and tools to safely handle or disassemble the payload if necessary, for return to the launch base. The payload recovery rate is exceptionally good and fast. A reflight is usually possible after minor refurbishment and replenishment of battery power.

### 3.2 Flight History

#### Flight H83-17

The first flight of the gravity-measurements experiment was scheduled for 17 September 1983 at Holloman AFB, NM. Predicted launch winds were very favorable, all prelaunch systems tests were "go," and the balloon was inflated at Nenninger Site on Holloman AFB, NM. Immediately after the balloon bubble was released, however, the launch-arm operator observed a long tear in the uninflated material, and the balloon developed a large sail. The crane holding the gondola backed away from the launch arm and dropped the gondola. The sailing balloon's lift in one direction, and the opposite pull of the crane, had resulted in very high tension at the hydraulic boom holding the gondola. Subsequent investigation showed that under that tension the boom would extend several feet, causing the payload-release mechanism to open. Although the shell of the cylindrical gondola was badly damaged, it had provided excellent protection for the instrumentation

inside; all of the sensors and electronics survived unimpaired. The crane malfunction was corrected, the gondola was refurbished, and the flight was rescheduled for October 1983.

#### Flight H83-19

All of the instrumentation was thoroughly retested and reassembled in the gondola. Early in the morning of 11 October 1983 the preflight checkout was completed smoothly, and the balloon and gondola (Figures 3.1 and 3.2) were transported to the Nenninger (launch) Site. As the 0600 Local Time launch hour approached, the Pibal runs at 15-min intervals were indicating that although surface winds were not exceeding the 10 to 12 knot limit for this launch, the low-level winds were increasing to unacceptable speeds. The flight meteorologist predicted a short interval of relative calm shortly after sunrise, and inflation was delayed accordingly. The predicted improvement in low-level winds did, in fact, occur, the balloon was inflated (Figure 3.3), and the launch maneuver was skillfully executed at 0811 Local Time, with the crane running the full extent off the paved site. The ascending balloon (Figure 3.4) traveled approximately southeast until, just before it entered float phase at 1004 Local Time, it abruptly changed heading and continued roughly northeast until the flight was terminated. The flight path is shown in Figure 3.5. Two hours of data were recorded at the 100,000 ft float level; then, by commanded gas valving, and some judicious pouring of ballast, the balloon was nudged into the 83,000 ft level. Its float motion there, however, was somewhat disturbed, and at 1430 Local Time the termination command was given to separate the gondola-parachute train from the balloon. The parachute recovery system had purposely been designed for low-g impact, using a 100-ft diam, flat circular parachute; consequently, the descent time was unusually long. The descent was observed by radar down to 35,000 ft at 2015. Ground impact was recorded by the chase aircraft at 2124. The gondola landed in a plowed field, just off a road, southeast of Lovington, NM, and was recovered in excellent condition.

## 4. DATA ANALYSIS

### 4.1 Objectives

The primary objective of a feasibility experiment is to answer the question "Can it be done?" The other objectives generally include an attempt to actually "do it" as well as possible, with appropriate caveats and limitations. In this project, a great deal of data were collected, organized, inspected, and analyzed by several different people and/or groups. Since this first flight was a feasibility

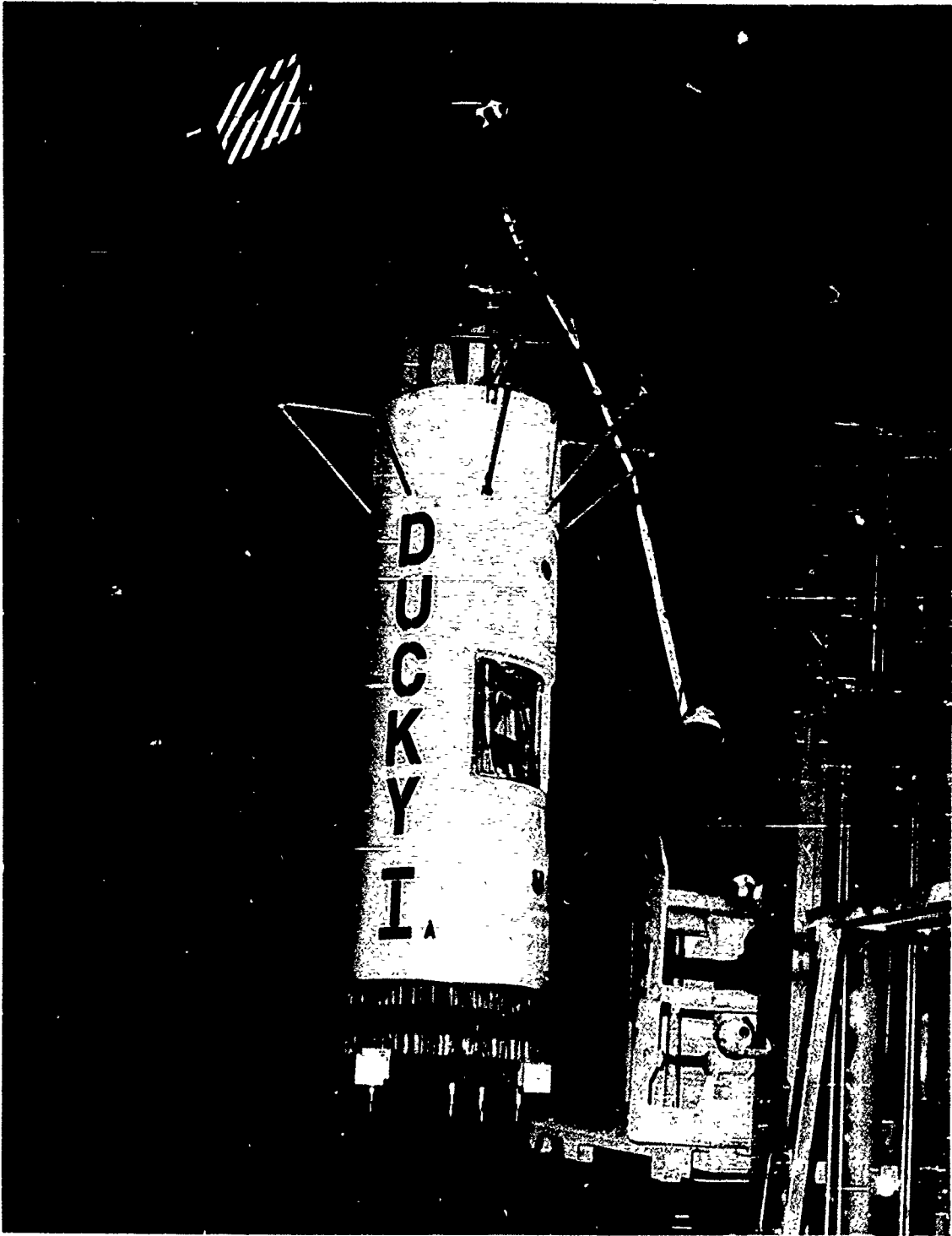


Figure 3.1 A Photograph of the Payload, named DUCKY Ia, Just After Transport to the Launch Site

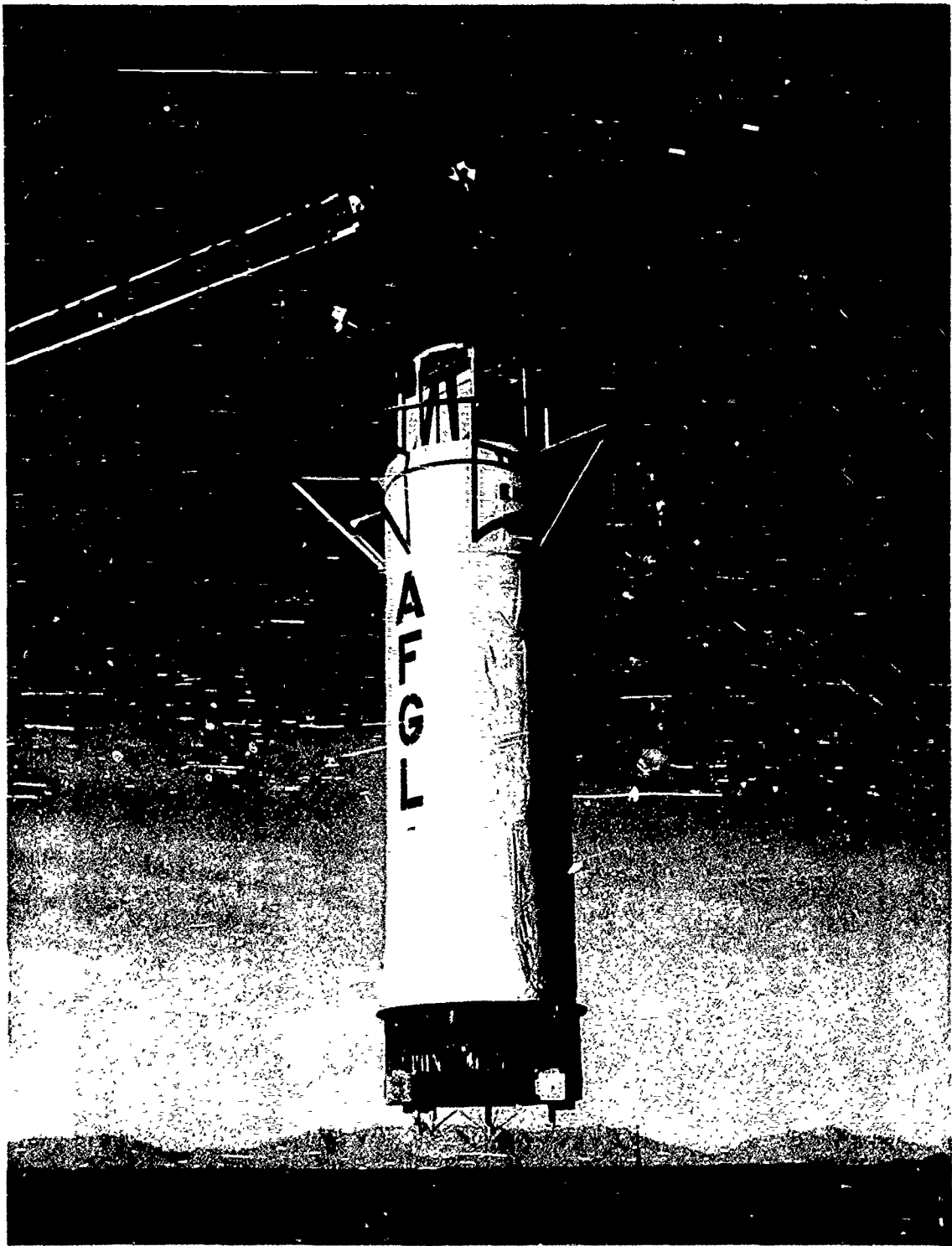


Figure 3.2 A Photograph of the Payload, Tested and Ready for Flight, at the Launch Site



Figure 3.3 A View of the Balloon Inflation With DUCKY Ia in the Background



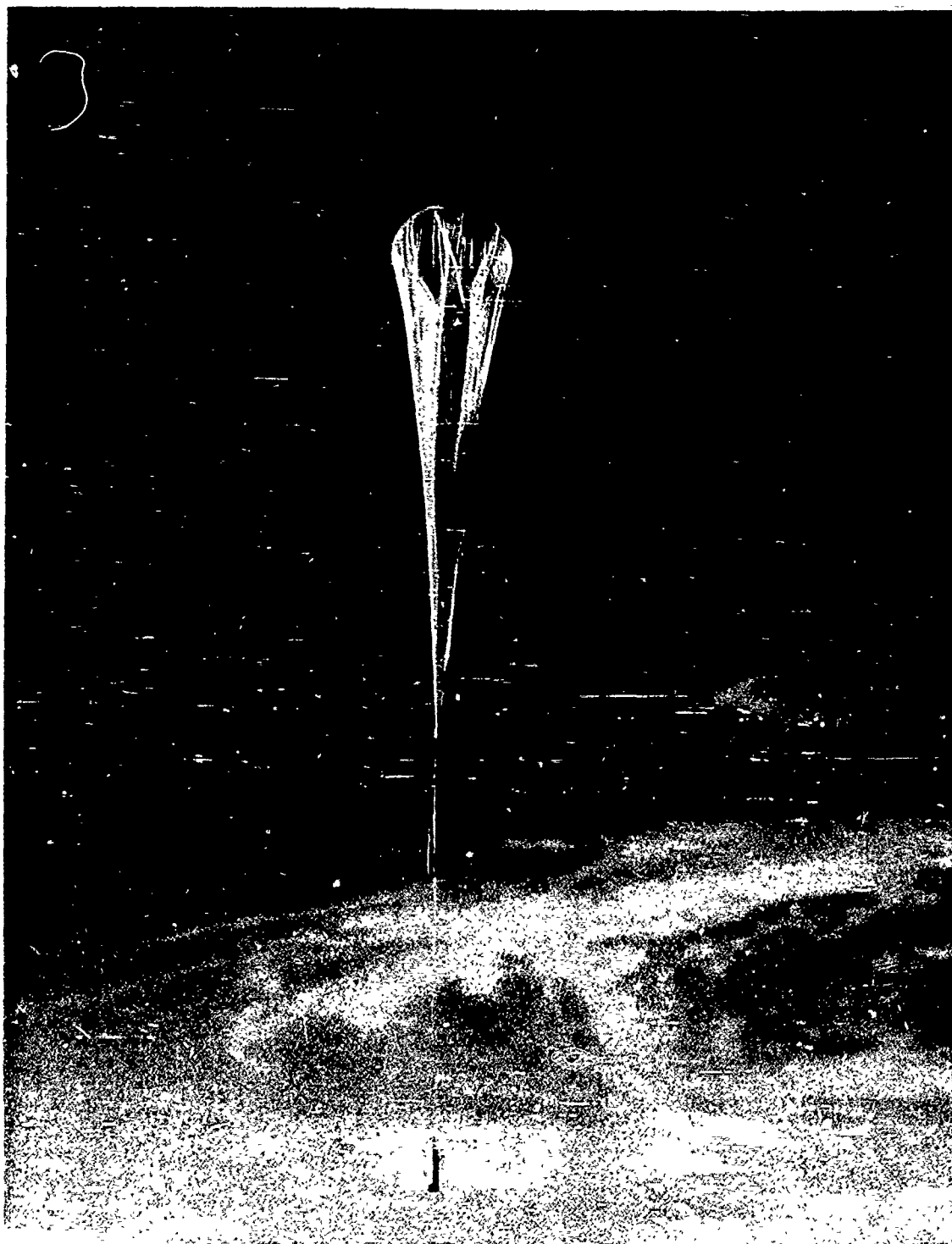


Figure 3.4 A Photograph of DUCKY Ia Minutes After Launch. For scale, the balloon-gondola system is about 400 ft from top to bottom

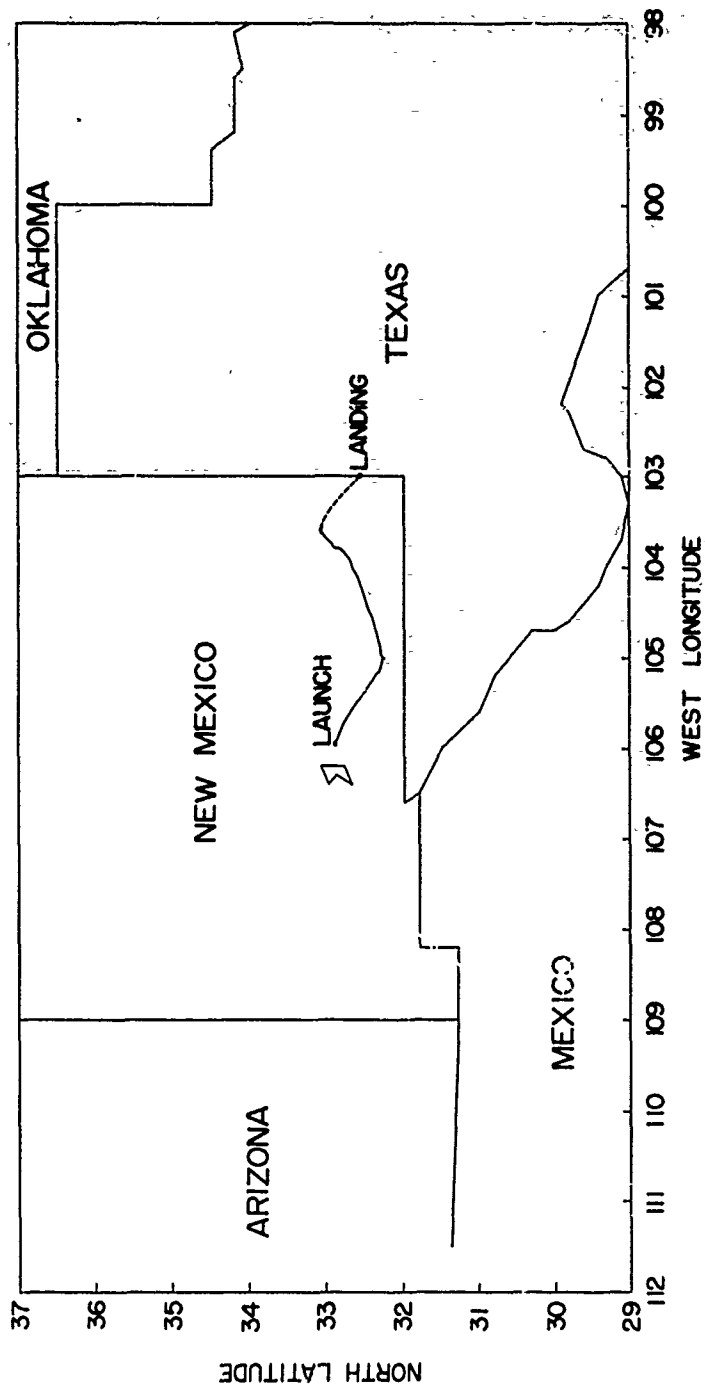


Figure 3.5 A Plot of the Flight Path of DUCKY 1a. The dashed line shows the path during descent

flight, the results are neither rigorous nor conclusive. With this view, assembling the existing data analysis into a coherent and organized package is difficult. The current objectives fall into two broad groups: 1) How good are the data, and what should be done on subsequent flights to improve the data quality? and 2) What is the measured gravity, and how do the measurements compare with mathematical models?

An overview of the data is shown in Figures 4.1 and 4.2. The former shows the altitude profile and raw gravimeter data for the entire flight; the latter shows the same, but only during float. Note that there are two "quiet" periods, just before 11 A.M. and just before 12 P.M., local time. Most of the data analysis that follows focuses on the second quiet time as it also showed the least rotation about the vertical axis. The strategy is to understand a short segment of "quiet" data before attempting to analyze the entire flight. In the end, enough was learned from this analysis to justify and contribute to a second flight.

The most important point for understanding the data analysis issues is that this really is a complex navigation problem. A complete solution requires a thorough understanding of not only the geophysics of gravity and gravity modeling, but also of navigation systems and analysis techniques. The analysis to be presented here is intended to illuminate the obvious problems and solutions to be addressed, and does not come anywhere near a complete solution. Part of the reason for that is due to the great amount of effort that was required just to assess the raw-data quality and assemble that data into an organized investigator tape; and part is due to the severe limitations resulting from unsatisfactory tracking data that undermined the only "ground truth" data available. Nevertheless, significant progress was made resulting in improved understanding of balloon dynamics, gravity measurements (although not to required accuracy), and the improved design of the gondola and instruments for subsequent flights.

The data analysis divides into roughly two parts; corrections for translational motions, and corrections for rotational motions. The translational motions are derived from the radar-tracking data, and have been "smoothed" in the vertical direction using a Kalman Filter with the vertical accelerometer data as additional input. This procedure used the higher frequency components of the accelerometer data only, minimizing the low-frequency components. Thus, we believe we have avoided the "chicken-and-the-egg" problem, since it is the lowest frequency component of vertical acceleration that we are after. Rotational corrections were not made due to lack of appropriate navigation software. However, the gyro and magnetometer data were inspected to give an indication of vertical angle errors, and thus the stability of the gondola. The direct purpose of such an inspection is to determine the need for a stabilized platform in future flights.

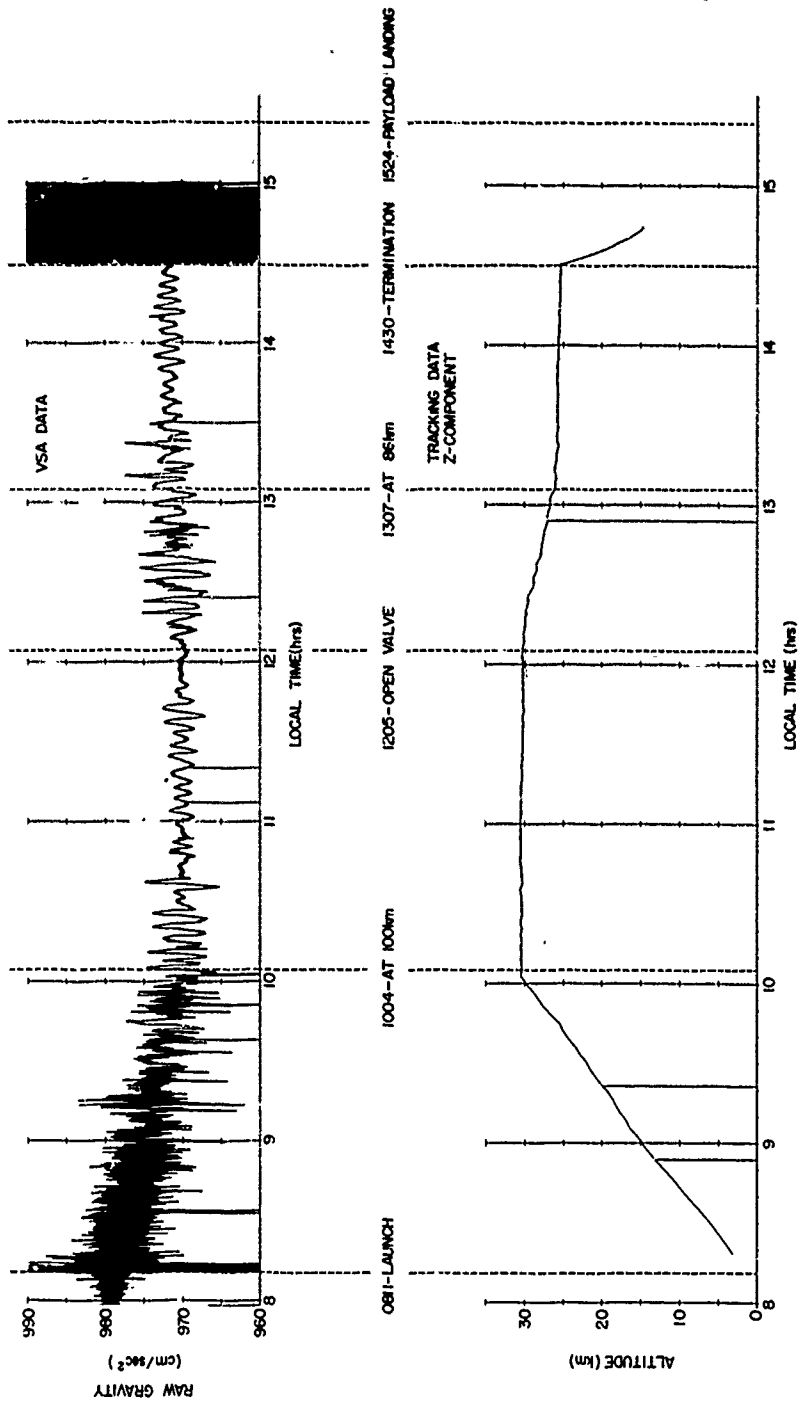


Figure 4.1 A Comparison of Flight Altitude and Gravimeter Measurements for the Entire Flight

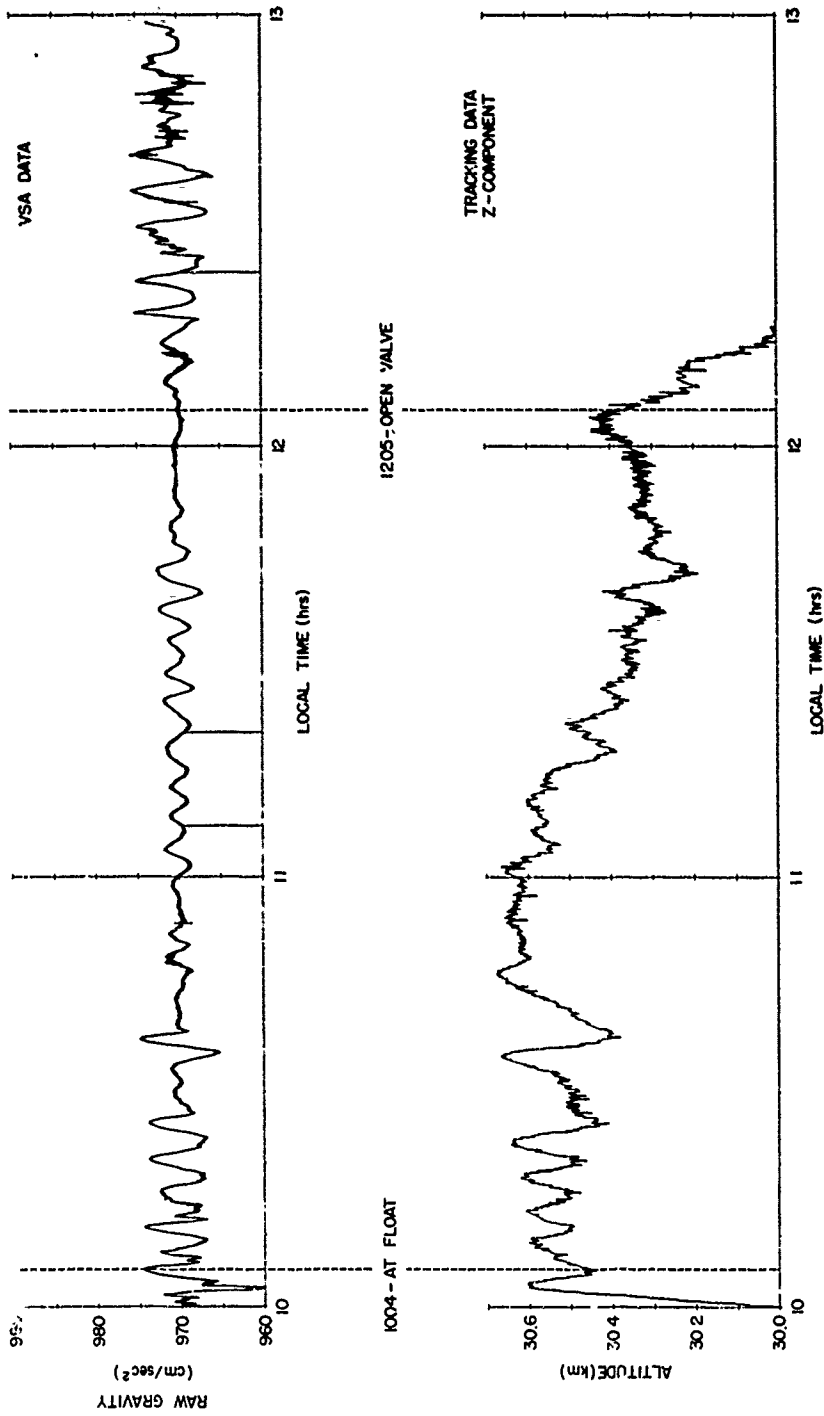


Figure 4.2 A Comparison of Flight Altitude and Gravimeter Measurements at Float Altitude Only

## 4.2 Prediction Filter to Fill in Gaps of Radar-Tracking Data

### 4.2.1 INTRODUCTION

One of the problems encountered during the post-flight data analysis was the existence of numerous data gaps in the WSMR radar-tracking data. The presence of gaps in the data can cause severe problems for tracking algorithms, and may have caused problems for DMA in deriving gravity estimate values from tracking data. For these reasons, an algorithm was developed to predict the missing data to preserve its continuity.

Sixty-one gaps were identified, ranging from 2 to 30 samples in length. In addition, three large gaps were identified that were 259, 199, and 839 samples long. Because of their length, these gaps were not filled since the performance of any algorithm would be highly suspect over such long periods.

In the next section we present the algorithm used to predict the missing data. This algorithm is based on the theory of linear prediction.<sup>6</sup> Following a discussion of the algorithm, a brief discussion of its implementation and some graphical results are presented.

### 4.2.2 LINEAR PREDICTION ALGORITHM

The approach taken to fill in the gaps is to use the technique of linear prediction. This technique assumes an auto-regressive (AR) time series model for the data, and uses this model to predict the missing data based on the existing data surrounding the gap. The signal  $x(n)$  is assumed to be a linear combination of past values and some input  $u(n)$ :

$$x(n) = \sum_{k=1}^P a_k x(n-k) + u(n) \quad (4.1)$$

The input  $u(n)$  is assumed to be a white noise term with variance  $\sigma^2$ . The model order  $P$  must be estimated, and the AR coefficients  $\{a_k\}$  must be determined. Experiments with the tracking data showed that  $P=8$  is a good model order to use.

The sample values  $x(n_0)$ ,  $x(n_0+1)$ , ...,  $x(n_1)$  are assumed to be missing. Thus, the gap is  $L=n_1-n_0+1$  points wide.

The data immediately preceding the gap are used to estimate the forward prediction coefficients  $a_k$  via the Burg method.<sup>7</sup> This method is part of the basic

6. Makhoul, John (1975) Linear prediction: a tutorial review, Proc. IEEE 63 (No. 4).

7. Burg, John P. (1975) Maximum Entropy Spectral Analysis. Ph.D. Thesis, Stanford University.

I\*S\*P package under the function name LNP. Five-hundred points are used to form the estimates. These prediction coefficients are used in the following formula to yield the forward prediction data:

$$\hat{x}_f(n) = \sum_{k=1}^P a_k \hat{x}_f(n-k), \quad n=n_0, \dots, n_0+1 \quad (4.2)$$

where  $\hat{x}_f(n)=x(n)$  for  $n < n_0$ .

Similarly, the data immediately following the gap are used to estimate the backward prediction coefficients  $\{b_k\}$ . Again, the Burg method is used and 500 points are used to form the estimate. The backward prediction coefficients are used in the following formula to form the backward prediction data:

$$\hat{x}_b(n) = \sum_{k=1}^P b_k \hat{x}_b(n+k), \quad n=n_1, n_1-1, \dots, n_0 \quad (4.3)$$

where  $\hat{x}_b(n)=x(n)$  for  $n < n_1$ .

The final prediction estimate  $x(n)$  is formed by adding weighted versions of the forward and backward estimates. The weights are proportional to the error in the predictors, where the error will increase as  $n$  is farther away from  $n_0$  for the forward predictor, and  $n_1$  for the backward predictor. The final prediction equation is then given by:

$$x(n_0 + m) = \left| \frac{L-1-m}{L-1} \right| \hat{x}_f(n_0+m) + \left| \frac{m}{L-1} \right| \hat{x}_b(n_0+m), \quad m=0, 1, \dots, L-1. \quad (4.4)$$

#### 4.2.3 IMPLEMENTATION ISSUES

If the data have a DC offset and/or linear trend, they can cause errors in estimating the prediction coefficients, and will affect the prediction results adversely. Therefore, the DC offset and trend are removed from the data preceding the gap and from the data following the gap before estimating the prediction coefficients, and then forward and backward prediction coefficients are computed from the detrended data. Detrended forward and backward predictions are computed using Eqs. (4.2) and (4.3). Then the DC offset and trend are added back to the predictions, and the weighting in Eq. (4.4) is finally applied.

One problem that was encountered during the graphical inspection of the gaps was that, very often, the data immediately surrounding the gaps seemed to be suspect. This is shown in Figures 4.3, 4.4, and 4.5 where the gap is indicated by the two vertical lines. Note that Figures 4.4 and 4.5 show two gaps in the time span shown. These figures show that the data just before the gap and just after the gap are noisier than data further away from the gap. For this reason it was decided to extend the size of the gap (or to predict more points) for gaps that showed this tendency. Also displayed in Figures 4.3, 4.4, and 4.5 are the corresponding predictions. These are the smooth curves that pass over the gaps. In Figures 4.4 and 4.5 where two gaps are so closely located, the two are treated as a single gap.

#### 4.3 Kalman Filter Model for Smoothed Estimates of Balloon Position

In Section 4.2, we considered a Kalman Filter (KF) model for estimating balloon velocity and acceleration using radar-tracking data only. Inputs to this model were the radar position tracking observations and associated errors, which gave rather unbelievable results for velocity and acceleration. In looking at some of the observations we concluded that there was little chance that the balloon was actually doing what the observations implied, and that tracking position errors given to us on tape were overly optimistic. The reported errors were on the order of 2 to 4 m, but we felt they were much higher. Using these small tracking errors in the KF model meant that we assumed the observations were quite good, leading to less-than-perfect velocity and acceleration results. In this problem we use the KF again, but this time a heuristic estimate is made of the position errors, given the data, and the high-gain Z-accelerometer observations are incorporated as well. The attempt here is to reprocess the data and look at the smoothed position, velocity, and acceleration estimates, given observations of both balloon position and acceleration.

##### 4.3.1 KALMAN FILTER MODEL

Define the state vector

$$\underline{x}(k) = [x(k) \quad \dot{x}(k) \quad \ddot{x}(k)]^T \quad (4.5)$$

where  $x(k)$  is the balloon position at time  $k$ , and  $\dot{x}(k)$  and  $\ddot{x}(k)$  are the first and second derivatives, respectively. The state model for the KF is based on constant-acceleration model with random perturbations:



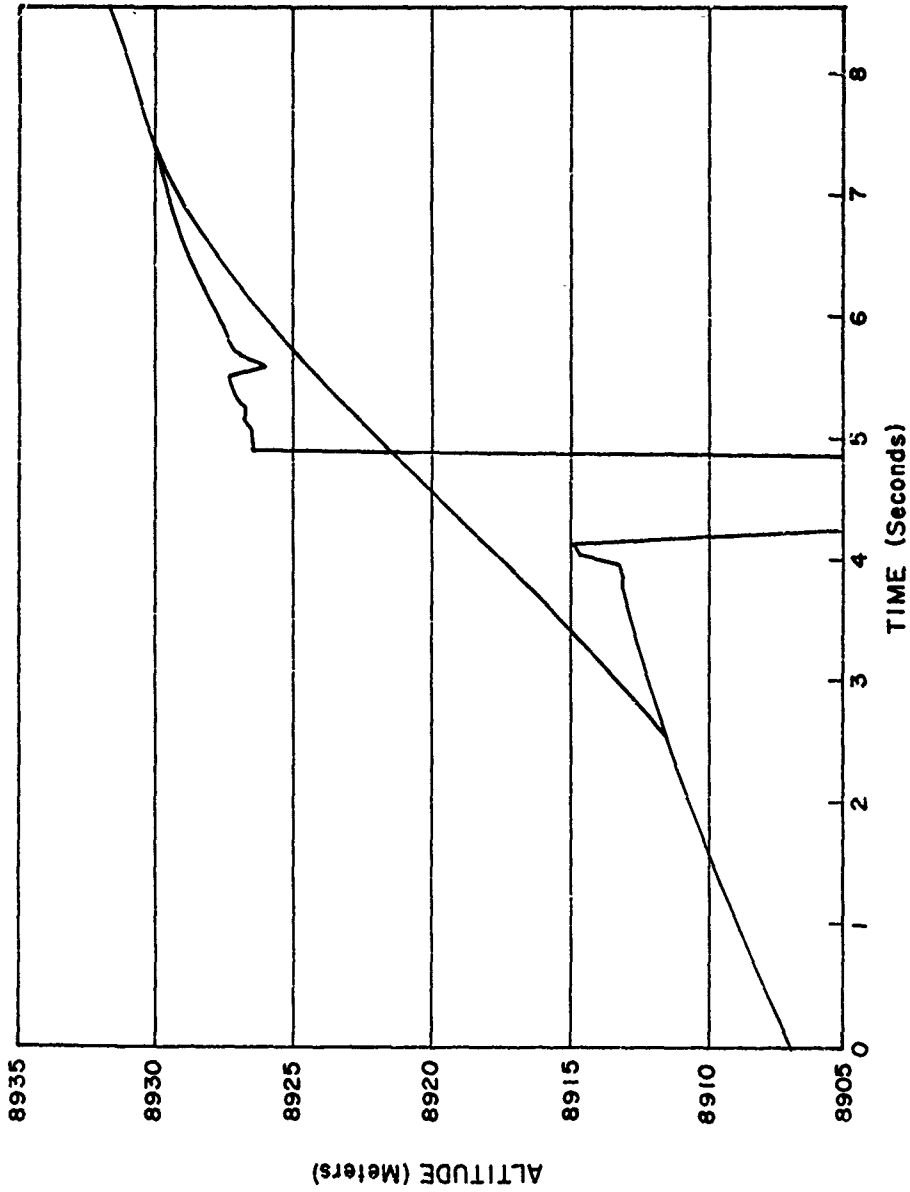


Figure 4.3 Example of a Gap of Eight Points in WSMR Tracking data. Gap is indicated by the two vertical lines in the plot. Also shown is the predicted data, which is the smooth line through the gap. Note that the predicted data actually spans more points than the gap alone, due to the larger fluctuations in the data surrounding the gap

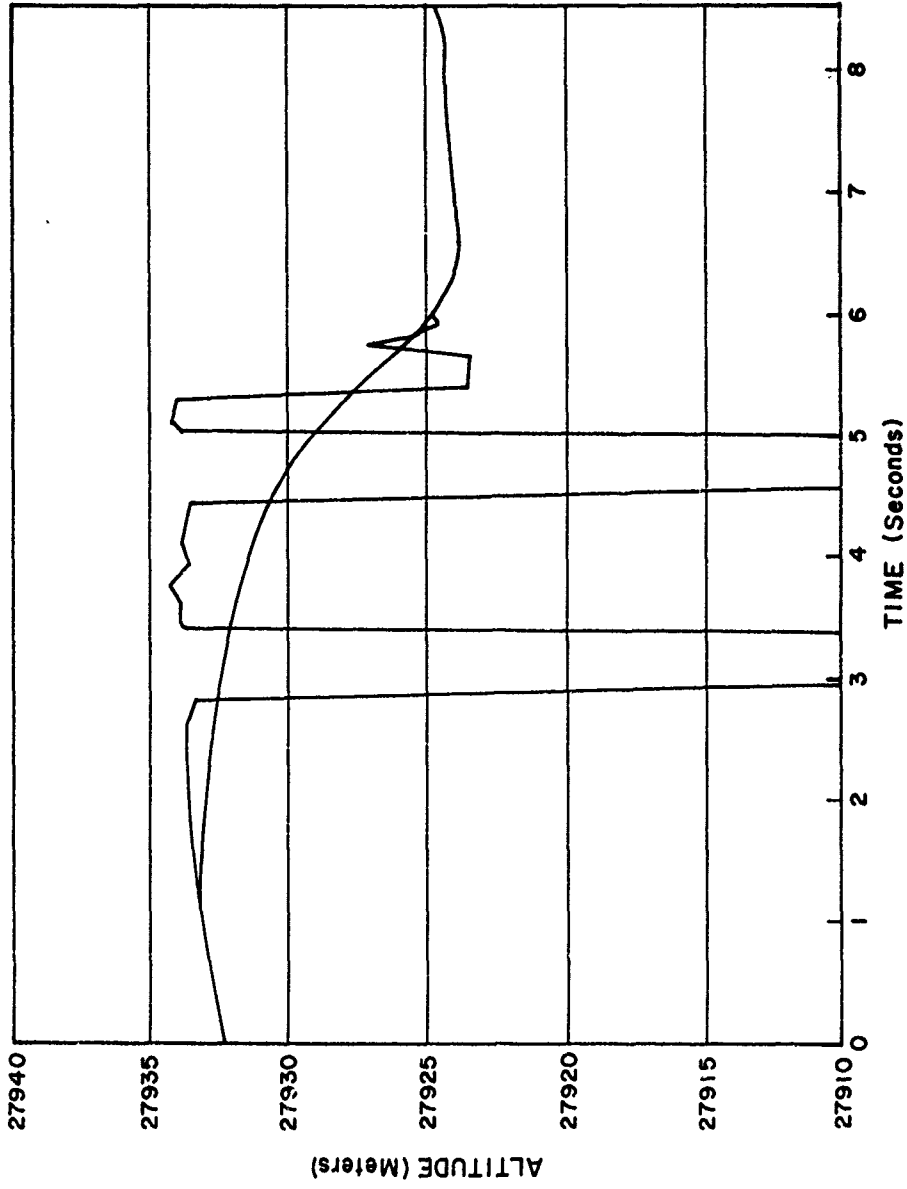


Figure 4.4 Example of Section of Data With Two Gaps, each of Length 6. Each gap is indicated by two vertical lines in the plot. Also shown is the predicted data, which is the smooth line through the gaps. Note that the predicted data actually spans more points than the gaps alone, due to the larger fluctuations in the data surrounding the gaps

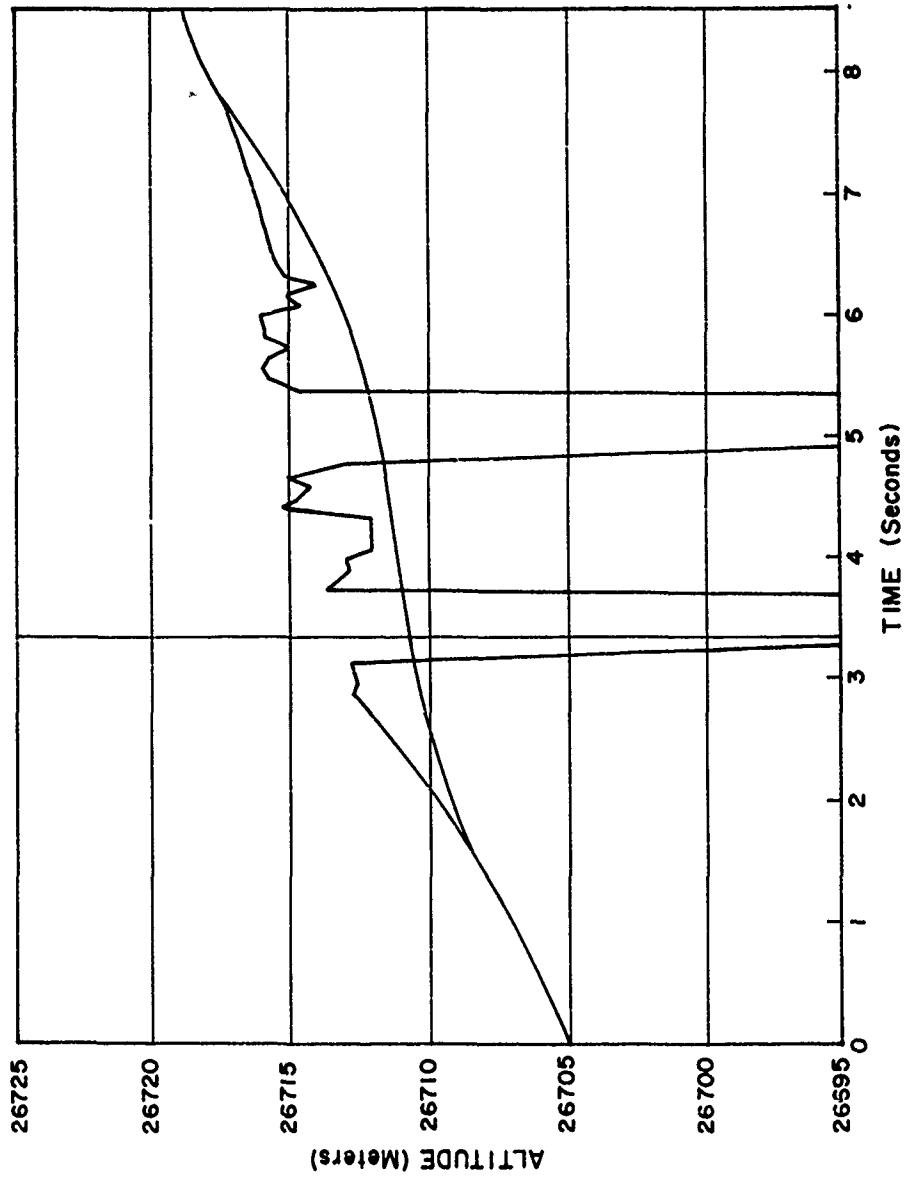


Figure 4.5 Example of Section of Data With Two Gaps, Each of Length 6. Each gap is indicated by two vertical lines in the plot. Also shown is the predicted data, which is the smooth line through the gaps. Note that the predicted data actually spans more points than the gaps alone, due to the larger fluctuations in the data surrounding the gaps

$$\underline{x}(k+1) = F\underline{x}(k) + G u(k) \quad (4.6)$$

where  $G = \begin{bmatrix} 0 \\ 0 \\ 1 \end{bmatrix}$  and  $F = \begin{bmatrix} 1 & \Delta & .5\Delta^2 \\ 0 & 1 & \Delta \\ 0 & 0 & \alpha \end{bmatrix}$  (system matrix) (4.7)

where  $\Delta$  is the sampling interval,  $\alpha$  is the acceleration parameter defining the bandwidth of acceleration, and  $u(k)$  is the driving white noise.

$$q = Q = E[u^2(k)] \quad (4.8)$$

is the white noise power. We are dealing with  $\Delta = .1$  sec and the parameters  $\alpha$  and  $q$  will be estimated from the data.

Observation Equation:

We observe the balloon position  $x(k)$  and acceleration  $\ddot{x}(k)$  so these are our observations  $\underline{z}(k)$ .

$$\underline{z}(k) = \begin{bmatrix} x(k) \\ \ddot{x}(k) \end{bmatrix} = H\underline{x}(k) + \underline{v}(k) \quad (4.9)$$

and  $H = \begin{bmatrix} 1 & 0 & 0 \\ 0 & 0 & 1 \end{bmatrix}$  (4.10)

where  $\underline{v}(k)$  is observation noise. Define

$$R(k) = E[\underline{v}(k)\underline{v}^T(k)] = \begin{bmatrix} r_1 & 0 \\ 0 & r_2 \end{bmatrix} \quad (4.11)$$

In our first KF attempt we used  $r_1=4$  (from the tracking-error tape), but this time we will make a heuristic estimate of  $r_1$  and  $r_2$ .

The Kalman Filter:

The KF performs a five-step iteration for each time  $k$ :

(1) State estimate extrapolation:

$$\hat{\underline{x}}_0(k+1) = F\hat{\underline{x}}_0(k) \quad (4.12)$$

where  $\hat{\underline{x}}(k)$  - state vector estimate  
 $\hat{\underline{x}}(k+i)$  - state vector estimate extrapolation

(2) Error covariance extrapolation:

$$P_0(k+1) = FP(k)F^T + GQG^T \quad (4.13)$$

where  $P(k) = E[(\hat{\underline{x}}(k) - \underline{x}(k))(\hat{\underline{x}}(k) - \underline{x}(k))^T]$  (4.14)

is the error covariance matrix, and  $P_0(k+1)$  is the error covariance matrix extrapolation

(3) Kalman gain computation:

$$K = P_0(k+1)H^T [HP_0(k+1)H^T + R]^{-1} \quad (4.15)$$

where  $K$  is the Kalman gain matrix,

(4) State estimate update:

$$\hat{\underline{x}}(k+1) = \hat{\underline{x}}_0(k+1) + K[z(k+1) - H\hat{\underline{x}}_0(k+1)] \quad (4.16)$$

(5) Error covariance update:

$$P(k+1) = [I - KH]P_0(k+1). \quad (4.17)$$

The block diagram form is shown in Figure 4.6.

#### 4.3.2 DATA USED AND PARAMETER SELECTION

The data used were a section of data from 1730-1807 zulu. The original 20 Hz Z-tracking data were decimated to 10 Hz for this problem. Plots of the detrended and DC bias-removed observations are shown in Figure 4.7. Note that in the lower figure the detrended Z-accelerometer data were multiplied by -1 to make the directions of the Z-axes the same. To select  $\alpha$  and  $g$ , we tried a few parameters, synthesized some data, and settled on the values:

$$\begin{aligned} \alpha &= 0.999 \\ q &= 2.5 * 10^{-7} \end{aligned} \quad (4.18)$$

To select  $r_1$  and  $r_2$  we looked at the observations. We selected a value of  $r_1 = 225 = 15^2 \text{ m}^2$  for the tracking data, and  $r_2 = 5 * 10^{-7} = (.0007 \text{ m/sec}^2)^2$ .

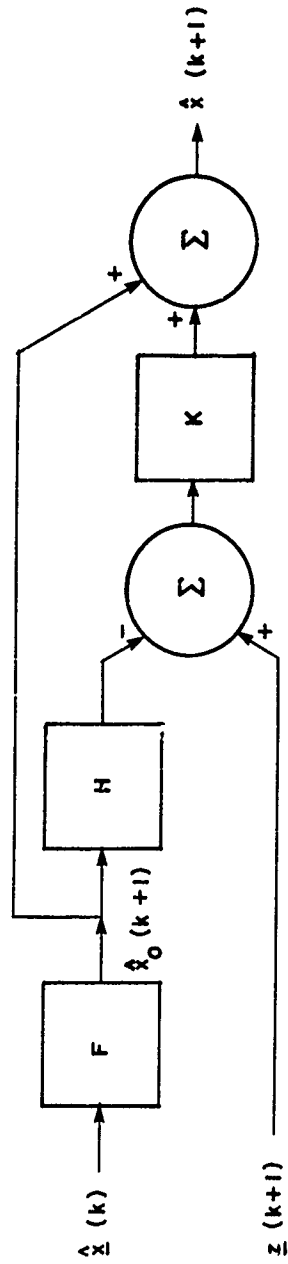


Figure 4.6 Block Diagram of Kalman Filter Used to Smooth Tracking Data Using the Flight Inertial System

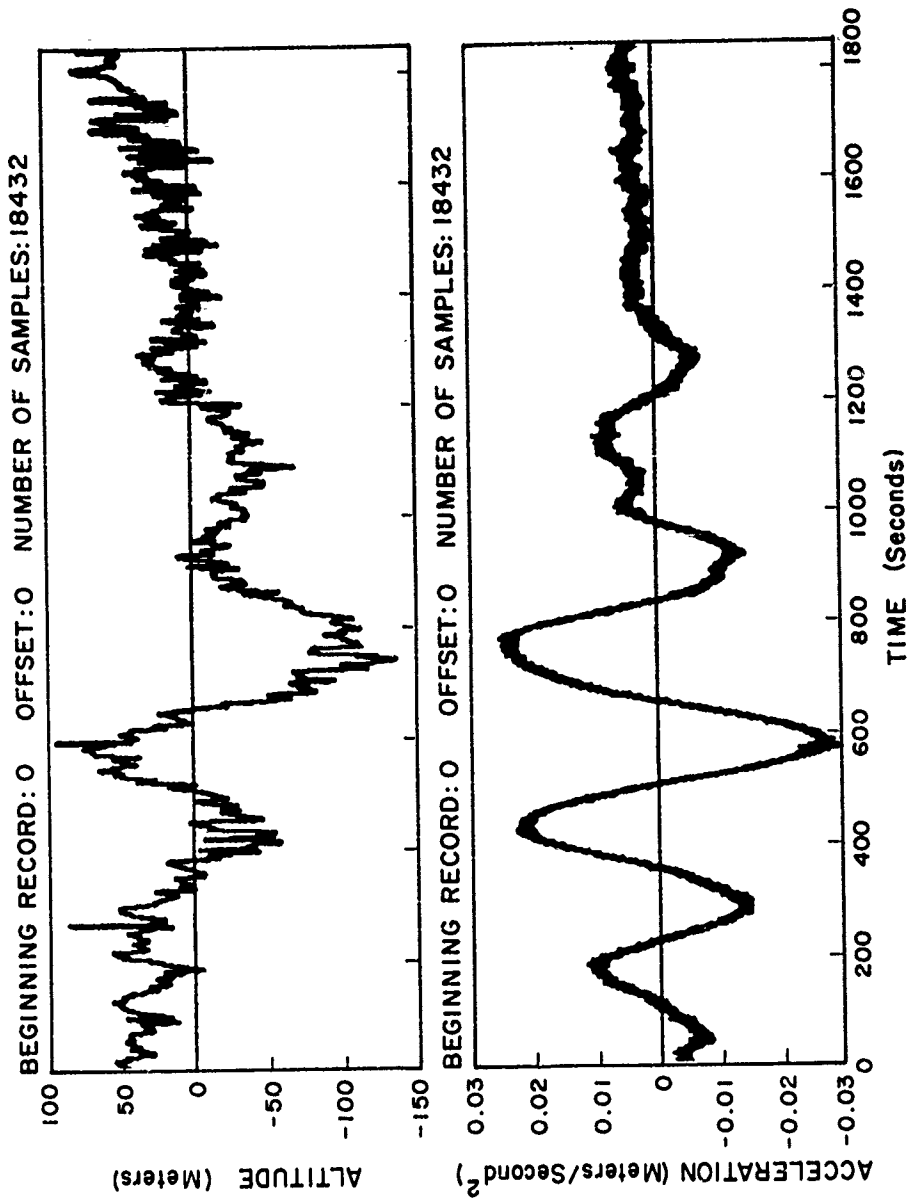


Figure 4.7 Plots of the Detrended Altitude and Vertical Acceleration for the Period of 1730 - 1807 Zulu. Note that the lower figure is inverted to make the positive Z for both plots in the same direction

### 4.3.3 RESULTS

The results of the KF output are shown in Figures 4.8, 4.9, and 4.10. In Figure 4.8 the tracking observations,  $x(k)$ , are plotted against the position estimate  $\hat{x}(k)$  for the first 204.8 sec of the file. Figure 4.9  $\hat{x}(k)$  and  $\overline{\hat{x}(k)}$  are plotted for the first 204.8 sec of the file. Finally, in Figure 4.10,  $\hat{x}(k)$  is plotted for the first 204.8 sec.

### 4.4 Recursive Estimation Approach to Signal Analysis

As part of the exploratory development effort, the balloon data were subjected to a brief analysis using the traditional approach of Wiener Filtering, or least-mean-square estimation. For a very large number of data points examined sequentially in time, the Wiener Filter can be constructed as a recursive digital algorithm. In the nonrecursive case, the Wiener Filter problem can be stated as follows:

Given a set of data points  $x_j$ ,  $j=1, 2, \dots, m$ , where each  $x_j$  consists of a signal  $S$  (in this case constant in time) plus additive uncorrelated zero-mean noise  $n_j$ , we wish to obtain a "best" estimate of the signal,  $\hat{S}$ , which can be written in general form as

$$\hat{S} = \sum_{j=1}^m h_j x_j \quad (4.19)$$

in other words,  $\hat{S}$  is a linear combination of all available data, and the problem at hand is to construct an algorithm that will generate the weighting coefficients  $h_j$  such that the  $\hat{S}$  so obtained is the "best" estimate of the signal  $S$ , with "best" left undefined in the most general sense. In the Wiener Filter approach, "best" is defined as that estimate of  $S$  which minimizes the mean-square-value of the error  $\epsilon$ :

$$E[\epsilon^2] = E[(S - \hat{S})^2] = E[(S - \sum_{j=1}^m h_j x_j)^2] \quad (4.20)$$

The usual approach is to differentiate the above expression with respect to each  $h_j$  and set equal to zero, resulting in a set of  $m$  equations in the unknowns  $h_j$ :

$$E[\epsilon x_j] = 0; \quad j = 1, 2, \dots, m. \quad (4.21)$$



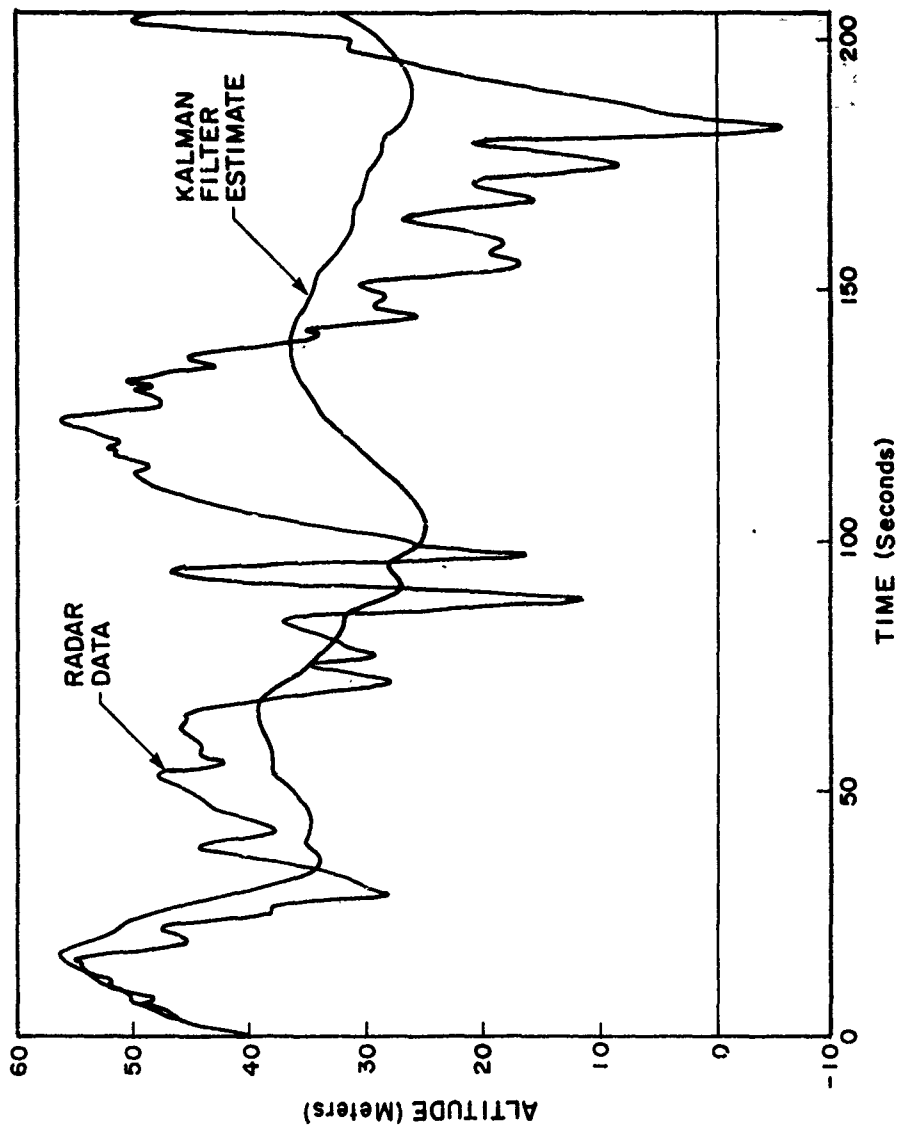


Figure 4.8 Comparison of Raw Radar Altitude Data With the Kalman Filter Output

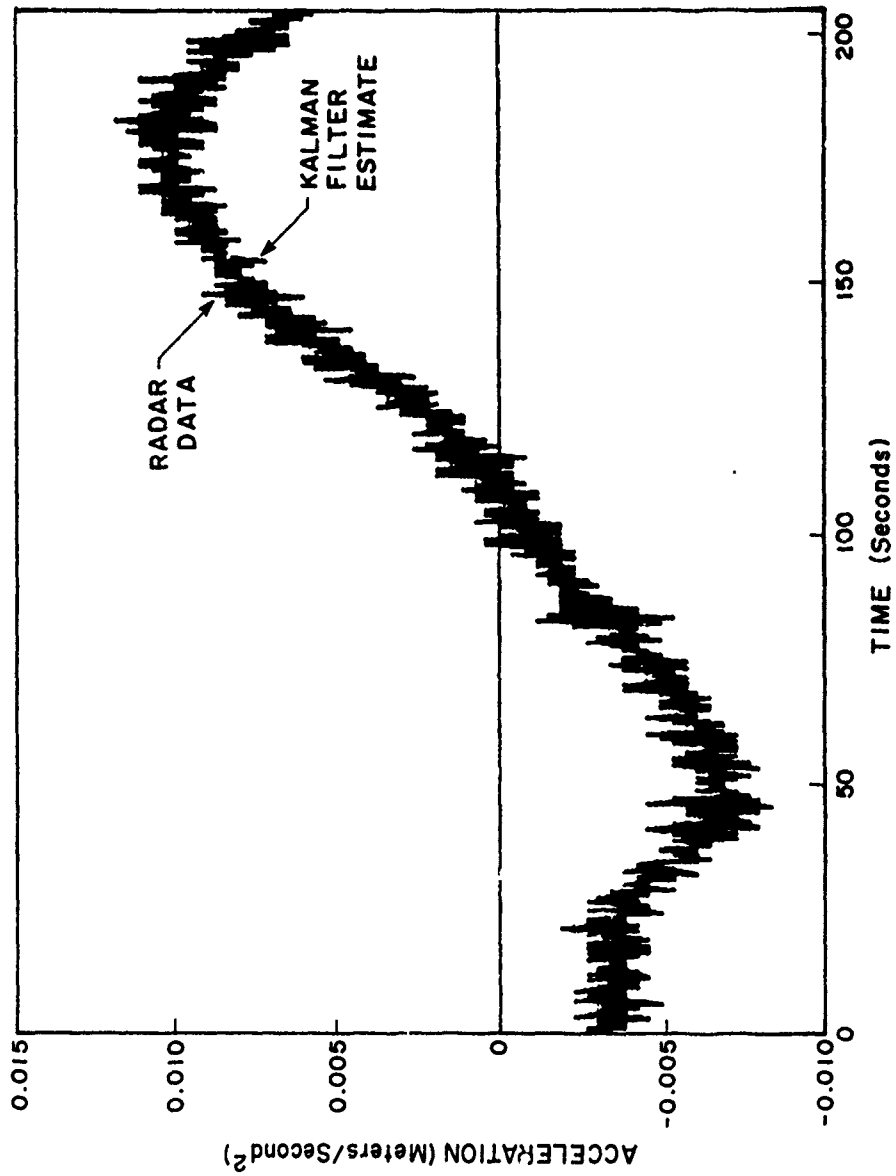


Figure 4.9 Comparison of Vertical Accelerations Sensed by the Flight Inertial System With the Kalman Filter Estimate

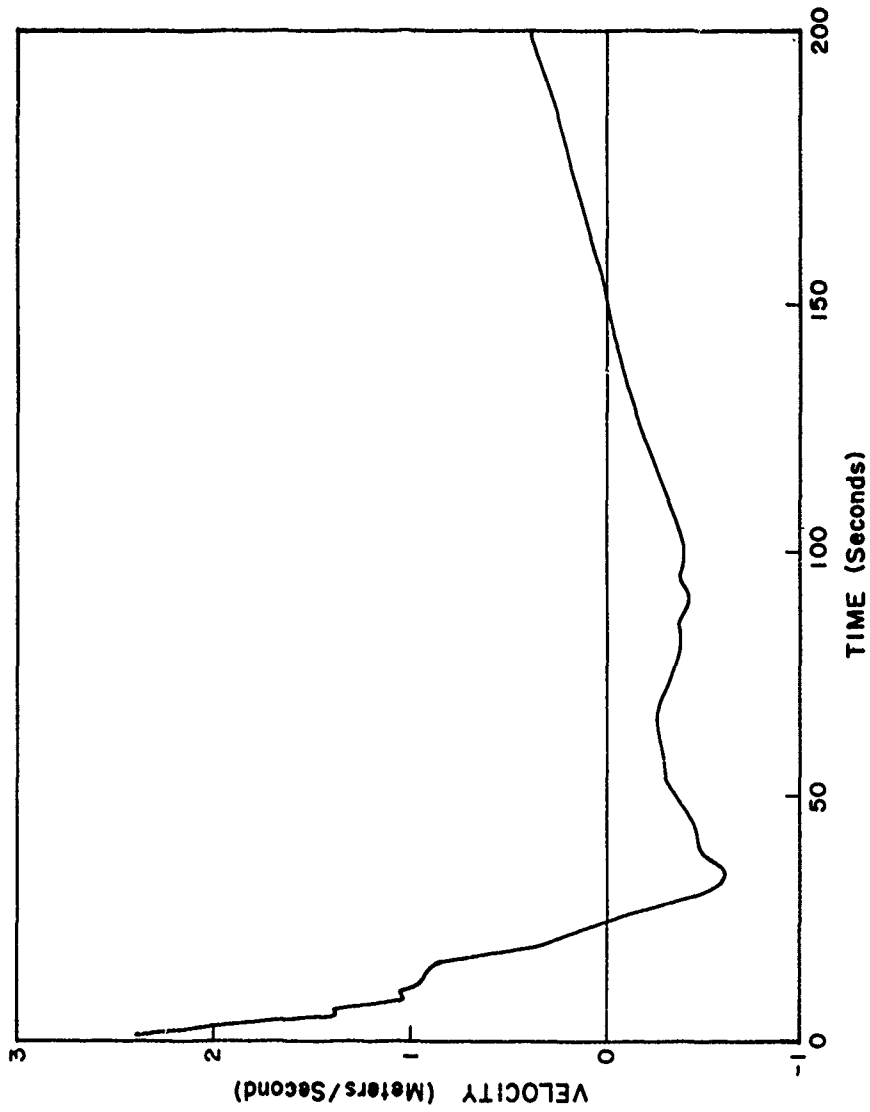


Figure 4.10 Comparison of Vertical Velocity Sensed by the Flight Inertial System With the Kalman Filter Estimate

The resulting matrix equation would have to be solved to obtain the coefficients that minimize  $E[\epsilon^2]$ . The set of coefficients becomes the Wiener Filter for this problem, and we can say that the data has been "passed through a Wiener Filter" to recover the best, or optimal, estimate  $\hat{S}$ .

For a large data set such as the balloon experiment, this approach would be unwieldy in the extreme. A variation of this approach, however, lends itself to optimal estimation using many noise-corrupted data points in sequence, that of recursive least-squares estimation. In this approach, the estimate is updated as each new data point is obtained, with the new estimate being the old estimate plus a weighted fraction of the difference between the old estimate and the new data:

$$\hat{S}_{k+1} = \hat{S}_k + b_{k+1}(x_{k+1} - \hat{S}_k), \quad (4.22)$$

where the obvious problem now is to obtain values for each  $b_k$  such that  $\hat{S}_k$  is the optimal estimate.<sup>8</sup>

Deriving the functional form of  $b_k$  is dependent on the characteristics of the physical process being modeled. In particular, if  $S$  is a time-independent random variable, that is, its value during data acquisition is constant but unknown, then recursive Wiener Filtering can be used, provided an appropriate form for  $b_k$  can be found. If, on the other hand, the signal is time-dependent (written  $S(t_k)$ ), then the optimal estimation process is embodied in the Kalman Filter, which can be written:

$$S_{t+1} = \phi_{t+1,t} S_t + G_t x_t, \quad (4.23)$$

which corresponds to the time-invariant recursive equation above with the substitutions

$$\phi_{t+1,t} = 1 - b_{k+1} \text{ and } G_t = b_{k+1} \quad (4.24)$$

In the Kalman Filter notation,  $S$  and  $x$  are system state and input vectors,  $G_t$  is the input matrix (set of input gain factors), and  $\phi_{t+1,t}$  is the transition, or system, matrix describing how the system state has changed from data point  $x(k)$  to data point  $x(k+1)$ .  $G_t$  and  $\phi_{t+1,t}$  are written with time subscripts to indicate that, unlike  $b_k$ , they are not time-invariant.

8. Schwartz, M., and Shaw, L. (1978) Signal Processing, McGraw-Hill, New York, Ch. 7.

In the absence of an analytic physical model, the form of the recursive weighting factor  $b_k$  is notably simple. The derivation for  $b_k$ <sup>8</sup> will not be given here; the functional form for a zero-slope estimate is simply

$$b_k = \frac{1}{k + b} = \frac{1}{k + \sigma_n^2/E[S^2]} \quad (4.25)$$

where  $\sigma_n^2$  is the variance, or power, of the additive noise and  $E[S^2]$  is the variance of the signal. For the gravimeter data application, however,  $E[S^2]$  is essentially zero, while  $\sigma_n^2$  is quite large and measurable. Signal power is, of course, close to zero, because the true value of  $g$  changes very slowly, and in very small fractional amounts, as the balloon describes its trajectory. Therefore, the noise-to-signal ratio  $b = \sigma_n^2/E[S^2]$  is extremely large, and a rough, practical approximation must be used for recursive estimation to be of any utility in this application.

In exploring possible processing approaches, various forms of  $b_k$  were evaluated, but none were found to be especially useful for the problem at hand. Specifically, the denominator of  $b_k$  was adjusted by: (1) assigning a heuristic value to  $b$ , the noise-to-signal ratio; (2) including a term to reflect signal slope in the neighborhood of  $x_k$ ; (3) including an additional term to reflect the deviation of  $x_k$  from the signal mean, normalized by  $\sigma_x$ ; and (4) several combinations of the three. Due largely to the nature of the data, however, (the signal being a constant "bias" with additive noise), recursive estimation gave results similar to simply calculating the mean of the data. Each data point used for both mean and recursive estimation gave results similar to simply calculating the mean. Each data point was corrected previously for two measurable error sources, altitude and Eotvos effect. The data was sampled at a 10 Hz rate, forming 10 files of 6144 samples (614.4 sec) on each of four channels: (1) VSA output, (2) altitude, (3) calculated Eotvos effect, and (4) reference DMA gravity estimates for the position at that time. The VSA and DMA reference channels were adjusted for a reference altitude of 30.300 km, with Eotvos applied to the VSA channel only. Thus, the total span of the data was 102.4 min in length; the recorded telemetry from 1630Z to 1810Z.

The results of this preliminary processing effort are tabulated in Table 4.1. Means and variances for each of the four channels are shown, plus recursive estimation results for three different forms of the coefficient  $b_k$ . The main points of this analysis are.

(1) Both the average and recursive estimate for individual files of 10.24 min in length show a very high level of variability; the average value of gravity  $g$

Table 4.1. Results From 10 Consecutive 10-sec Segments. Altitude is derived by Kalman smoothing of radar data and flight accelerometers. Eotvos is computed from radar data only. DMA gravity models are shown on raw form ( $g_1$ ), then continued to 30.3 km altitude and 970,000 mGals subtracted ( $g_2$ ). VSA data are shown on raw form (VSA), with 970,000 mGals subtracted ( $VSA_2$ ) and then continued to 30.3 km altitude with Eotvos corrections applied ( $VSA_3$ ). In principle,  $g_2$  and  $VSA_3$  show data as though the balloon were stationary at 30.3 km altitude with a 970,000 mGals bias removed. Instrument and processing noise is clearly evident. Although there are a number of ways to interpret these results, the best is to look at the 100-sec average

File	Altitude	Eotvos	$g_1$ (DMA) raw	$g_2$ (DMA) (g-970), 30.3 km	VSA raw	$VSA_2$ (g-970)	$VSA_3$ (g-970), 30.3 km, Eotvos
	$\frac{m}{\sigma}$	$\frac{mGals}{\sigma}$	$\frac{mGals}{\sigma}$	$\frac{mGals}{\sigma}$	$\frac{mGals}{\sigma}$	$\frac{mGals}{\sigma}$	$\frac{mGals}{\sigma}$
1	$\frac{30415}{84}$	$\frac{-43.1}{28.8}$	$\frac{970230}{46}$	$\frac{226.5}{3.9}$	$\frac{970142}{2003}$	$\frac{136.6}{2003}$	$\frac{215.4}{19.8}$
2	$\frac{30506}{67}$	$\frac{-57.3}{34.6}$	$\frac{970231}{66}$	$\frac{230.6}{4.0}$	$\frac{970000}{626}$	$\frac{3.0}{626}$	$\frac{123.7}{6.1}$
3	$\frac{30523}{14}$	$\frac{-82.8}{34.8}$	$\frac{970212}{54}$	$\frac{226.5}{3.6}$	$\frac{970144}{469}$	$\frac{151.6}{469}$	$\frac{303.3}{4.7}$
4	$\frac{30490}{27}$	$\frac{-84.6}{36.0}$	$\frac{970218}{48}$	$\frac{229.5}{4.1}$	$\frac{969980}{830}$	$\frac{-24.9}{830}$	$\frac{118.3}{8.2}$
5	$\frac{30400}{66}$	$\frac{-63.2}{46.4}$	$\frac{970226}{34}$	$\frac{227.9}{4.2}$	$\frac{970129}{811}$	$\frac{128.2}{811}$	$\frac{222.2}{8.0}$
6	$\frac{30288}{35}$	$\frac{-70.2}{45.9}$	$\frac{970285}{58}$	$\frac{223.9}{3.0}$	$\frac{920113}{970}$	$\frac{107.9}{970}$	$\frac{176.4}{9.6}$
7	$\frac{30256}{32}$	$\frac{-73.8}{47.7}$	$\frac{970290}{47}$	$\frac{230.1}{5.4}$	$\frac{969999}{1370}$	$\frac{-14.0}{1370}$	$\frac{46.3}{13.6}$
8	$\frac{30177}{23}$	$\frac{-73.8}{54.7}$	$\frac{970304}{46}$	$\frac{221.3}{7.6}$	$\frac{970328}{1026}$	$\frac{332.8}{1026}$	$\frac{368.5}{10.2}$
9	$\frac{30235}{23}$	$\frac{-77.6}{43.5}$	$\frac{970291}{47}$	$\frac{225.3}{4.3}$	$\frac{970225}{1763}$	$\frac{232.1}{1763}$	$\frac{290.0}{1.7}$
10	$\frac{30208}{78}$	$\frac{-92.4}{38.8}$	$\frac{970286}{36}$	$\frac{234.8}{7.1}$	$\frac{969973}{684}$	$\frac{-30.8}{684}$	$\frac{33.3}{6.8}$
Sum	_____	_____	_____	$\frac{227.6}{4.2}$	_____	_____	$\frac{189.7}{8.0}$

Average over 10 segments (100 seconds total) [g(DMA)-VSA] at 30.3 km =  $37.9 \pm 6.3$  mGals

(with a bias of 970 Gals removed) ranges from a low of 0.3325 Gals to a high of 0.36852 Gals, the gross average being 0.1897 Gals. However, when all 10 files are linked and recursive estimation is used for the entire data stream of 102.4 min, the variability drops to extremes of 0.1945 Gals to 0.2842 Gals, with a final estimate of 0.1963 Gals for one example.

(2) The best results with recursive estimation, shown in (1) above, were obtained by including an additional b-factor in the correction coefficient denominator, being the product of the average absolute value of local slope times one, plus the deviation of that data point from the segment mean, both quantities normalized by the segment standard deviation, the product then assigned an exponent of 8. This additional factor appeared to attenuate the noisiest segments of the data stream sufficiently to allow a small improvement in the final result for 'g'.

(3) The theoretical value of 'g' was obtained two different ways and was found to be in very good agreement. The average of the local height corrected DMA values, which include the upward continuation of surface anomalies, and a calculation of average 'g' at altitude using Table 11 of OSU Report #360,<sup>9</sup> both yielded a value of 0.227 for 'g' (970.227 Gals). This placed our preliminary experimental results approximately 30 to 35 mGals low in comparison with theory. This error could easily be accounted for by a slight vertical misalignment of the VSA, or by a bias in the electronics.

(4) An examination of Table 4.1 shows that the variance, or noise power, can be assigned almost entirely to the VSA channel, which on average is about 600 times the geometric average of the variances of the altitude and Eotvos channels, the two being comparable in noise-power content. An autocorrelation of the VSA channel reveals that virtually all the noise power lies in a narrow frequency band centered about a 280-sec oscillatory period, very close to the characteristic period of vertical oscillations of a fully inflated balloon in an isothermal atmosphere, typically calculated at about 255 sec.<sup>10</sup> Therefore, improved signal conditioning emphasizing narrowband noise smoothing should be of primary consideration in future flight-data analysis.

---

9. Cruz, J. Y., and Laskowski, P. (1984) Upward Continuation of Surface Gravity Anomalies, Report, 360, Dept. of Geodetic Science and Surveying, Ohio State Univ., AFGL-TR-84-0331, ADA154973.

10. Morris, A. L. (1975) Theory of balloon flight, Scientific Ballooning Handbook, NCAR-TN/IA-99, pp. II-34 to II-37.

## 4.5 Rotation

### 4.5.1 INTRODUCTION

All formal data analysis described thus far dealt with translational motions only, and are a summary of the best of many approaches tried. A complete solution requires proper application of strapdown inertial guidance concepts and gravity-data analysis. Since rotational analysis is complex, and mutual interaction among the different data sets, (including translational analysis), is nonlinear, such a complete solution does not exist yet. Short of processing all the data simultaneously, such as with an all-inclusive Kalman Filter, a rational approach requires solving the translational problems first, then approaching the rotational problems. The latter is described here qualitatively. Specifically, such insight is needed to design the data analysis scheme properly for subsequent flights.

### 4.5.2 INSTRUMENTS AND METHODS

Three sets of motion-sensing instruments were flown in addition to the gravimeter. They are the accelerometers, the rate gyros, and the magnetometer; all three-axis instruments. All give useful information about gondola rotational motions. As high-frequency (greater than 0.1 Hz) noise has not yet been properly characterized, a 0.1 Hz, Low-Pass, Zero-Phase Shift Butterworth Filter was applied to the data. Thus, the principal signals evident are of periods longer than 10 sec. Raw data will be shown in the figures for background information only.

#### Accelerometers

The three-axis accelerometer on board is oriented with Z up, X out the front door, and Y the orthogonal axis in a right-handed system. We start with the concept of the "true vertical," which is the local perpendicular to the geoid and is the locally stable direction which the gondola system sees as "down." Since the gondola system has alignment errors (static), and kinematic motions (dynamic), the gondola axis is generally not aligned with the true vertical.

The vector sum of the three accelerometers is in a direction, and has a magnitude that must be the vector sum of the gravitational acceleration (true vertical) and the instantaneous kinematic acceleration. Since the gondola cannot turn upside down, and it does act as a pendulum which has a restoring force in the direction of the gravity vertical, then to first approximation, the average vector sum of the accelerometers is in the direction of the true vertical. Applying a forcing function (e.g., wind, atmospheric density variations) to the balloon system will alter the measured accelerations, but unless the forcing function is applied for a period of time comparable to the averaging period, the average direction of kinetic acceleration must still be zero. The horizontal accelerations



are immediately countered with a restoring force from pendulous swing, while the vertical accelerations are countered when the balloon achieves its new float altitude. Thus, we expect that over a few seconds or more, the horizontal accelerations will average to zero, but the vertical may not. In both cases, the sensed accelerations still average to the direction of the true vertical. Affecting both direction and magnitude are axis misalignments, biases, and drifts of the individual sensors. All these considerations apply for translational motion only; they are significantly more complicated when rotation aspects are included. Any rotation adds centrifugal or centripetal acceleration in a variety of directions, and coning (i.e., the motion of a given accelerometer axis describing a cone) is a real concern.

Combining all of the above effects, the vector sum of the accelerometers generally points in the direction of the gravity vertical, but the components of that vector are contaminated by axis misalignments, biases, and rotational motions. Any differences detected between the Z-accelerometer vector and the accelerometer vector sum must be attributed to a combination of all these effects.

The one identified kinematic acceleration that does not average to zero is due to pendulum motion. Such swinging adds an average acceleration component along the pendulum axis (where the measurements are done in a strapdown system), thus adding to the apparent measured acceleration in the direction of the true vertical. The equations describing the average acceleration are:

$$a_r(\text{avg}) = g [3 \sin \theta_0 / \theta_0 - 2 \cos \theta_0] \quad (4.26)$$

$$a_z(\text{avg}) = g [3 - (\cos \theta_0 / \theta_0)(2 \ln \tan(P/4 + \theta_0/2))] \quad (4.27)$$

where  $a_r$  and  $a_z$  are the radial (along the pendulum line) and vertical accelerations, respectively,  $g$  is the ambient gravitational acceleration, and  $\theta_0$  is the maximum swing angle. Figure 4.11 plots the  $a_r$  and  $a_z$  for a maximum swing angle  $\theta_0$ .

A comparison of the individual accelerometer signals, then transformed into spherical coordinates, is shown in Figure 4.12, with a smoothed version shown in Figure 4.13. These data are for the 102.4 sec period during the quiet time. During this time, the vector sum shows a total acceleration varying over about 500 mGals. The Z-axis misalignment is about 0.2 deg with a variation of less than 0.01 deg. Filtering with the 0.1 Hz low-pass filter lowers the apparent variation to 0.001 deg. The simplest way to look at this is to think of an overall Z-axis

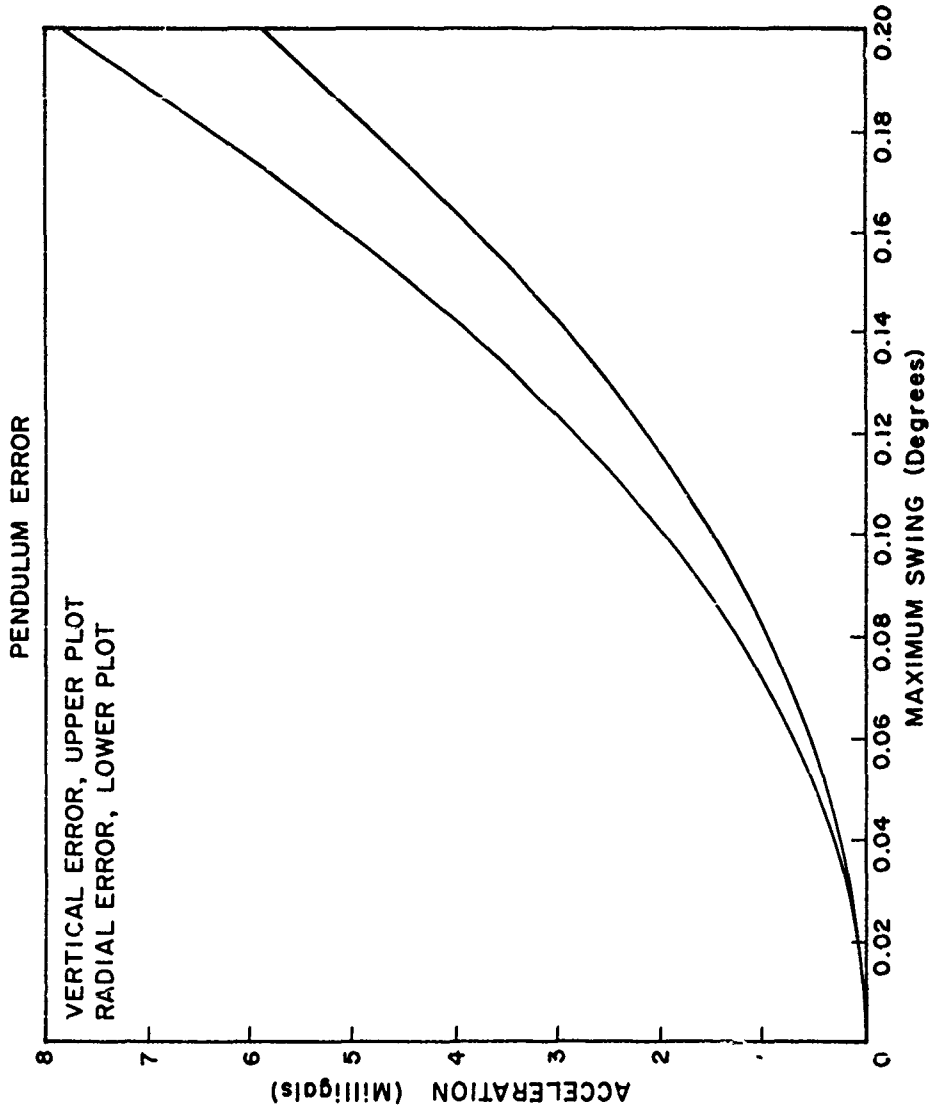


Figure 4.11 A Plot Showing Measured Gravimeter Error Due to Pendulum Swing. Radial error is along the pendulum line, vertical is corrected to true vertical

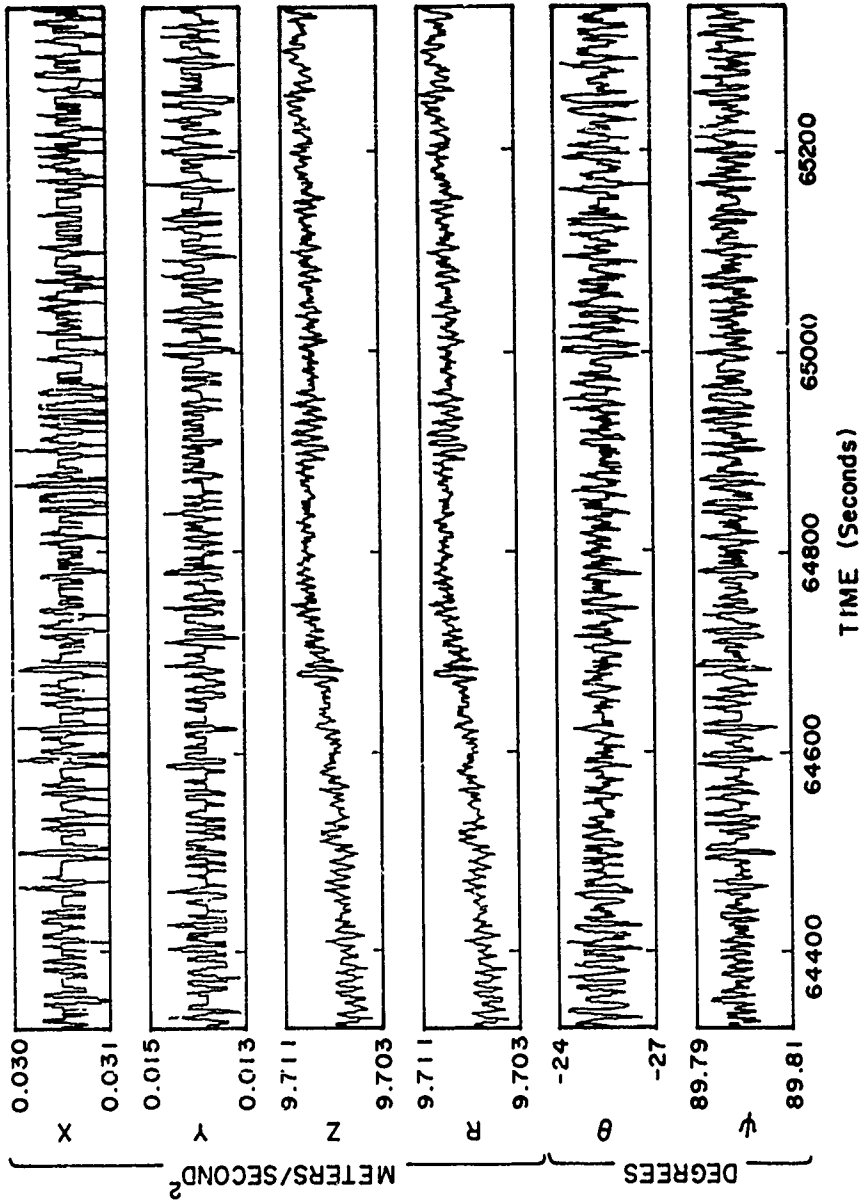


Figure 4.12 Example of Raw 3-Axis Accelerometer Error in Cartesian and Spherical Coordinates

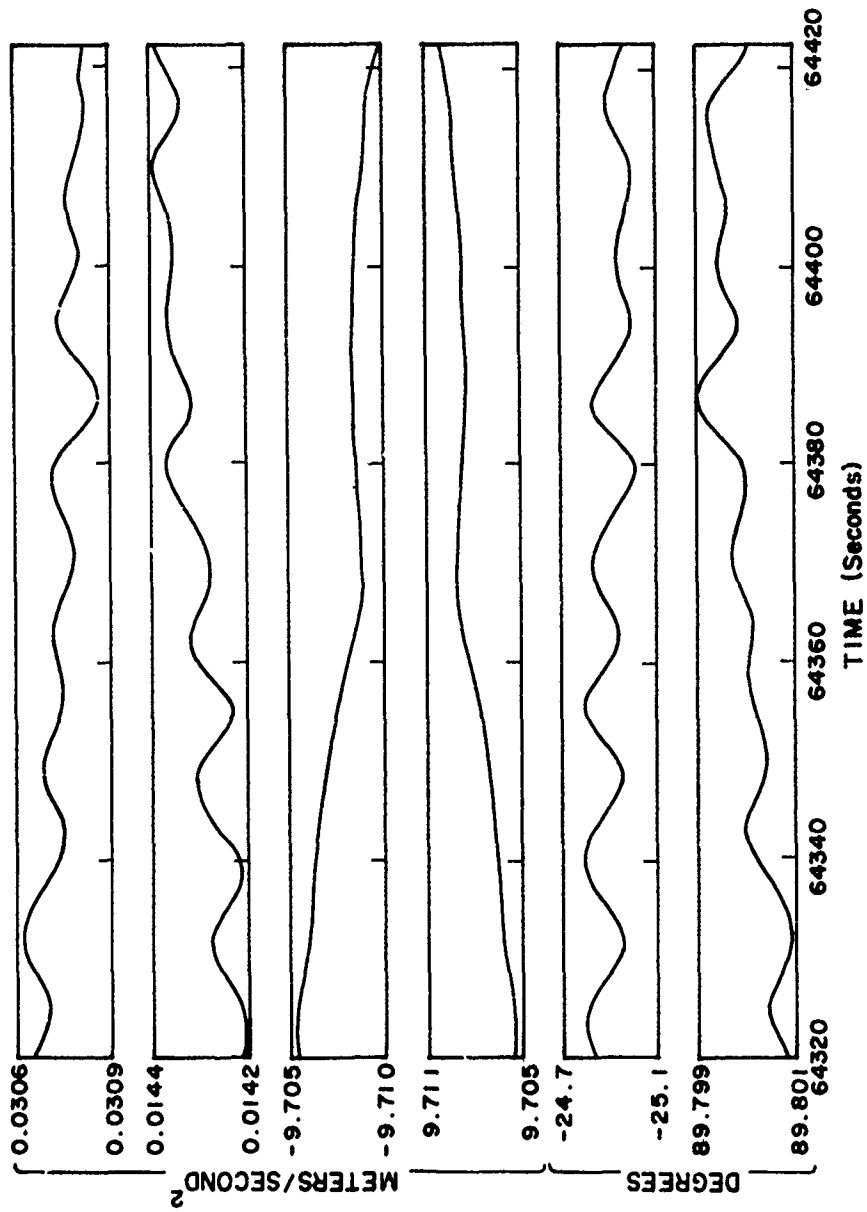


Figure 4.13 Example of Smoothed 3-Axis Accelerometer Error in Cartesian and Spherical Coordinates

misalignment of 0.2 deg with a pendulous swing of 0.01 deg. The error due to the misalignment is:

$$\overline{\Delta g} = g (1 - \cos \theta_1) \quad (4.28)$$

where  $\Delta g$  is the error in mGals,  $g$  is the gravitational acceleration in mGals and  $\theta_1$  is the alignment-error angle. From Figures 4.11 and 4.12, and Eq. 4.28, the latter introduces an error of much less than 1 mGal, while the misalignment introduces an error of -6 mGals. The sum of the average errors due to misalignment and pendulum swinging is then about -6 mGals.

#### Rate Gyros

The gondola gyros also form an orthogonal system. To a first approximation, the Z-gyro shows rotation about the gondola axis, including the effect of the coupling of angular momentum between the balloon and gondola. To be more accurate, it is necessary to convert the gyro data into an inertial coordinate system. The proper approach is through the use of Euler angles. Although some progress has been made in this area, for this report we do not consider Euler angles, but look at the raw data alone. From a practical point of view, the X-axis and the Y-axis gyros must average to zero, as the gondola cannot turn upside down, or even depart significantly from vertical for any significant amount of time. This is not what we see in the data (Figures 4.14 and 4.15), however. What the X- and Y-gyros do show is a bias which must be incorrect; therefore, the data can reasonably be detrended. Given that two gyros have biases, we must assume that the Z-gyro is also biased. The magnetometers and the compass can be used to calibrate the Z-gyro by computing the angle to magnetic North and differentiating. Thus, in principle, we have a way to compensate for the biases in all three gyros.

#### Magnetometers

Finally, the gondola package contains a three-axis magnetometer and a compass. These instruments can be used to gain information on rotational aspects of the gondola since, given a good earth's magnetic field model, the data will yield absolute angle. Mathematical continuation models also apply to magnetic fields, and the magnetic data available here at 30 km altitude is unique and may form a rather unique data set. These instruments give a complementary data set to the rate gyros, and allow for consistency checks and noise analysis.

Two sets of data are presented to show three-axis rotation of the gondola: the compass data showing rotation about the gondola Z-axis, and the magnetometers showing all three axes. Figure 4.16 shows the angle between the gondola X-axis and magnetic North for the compass, and between the X-axis and true North for

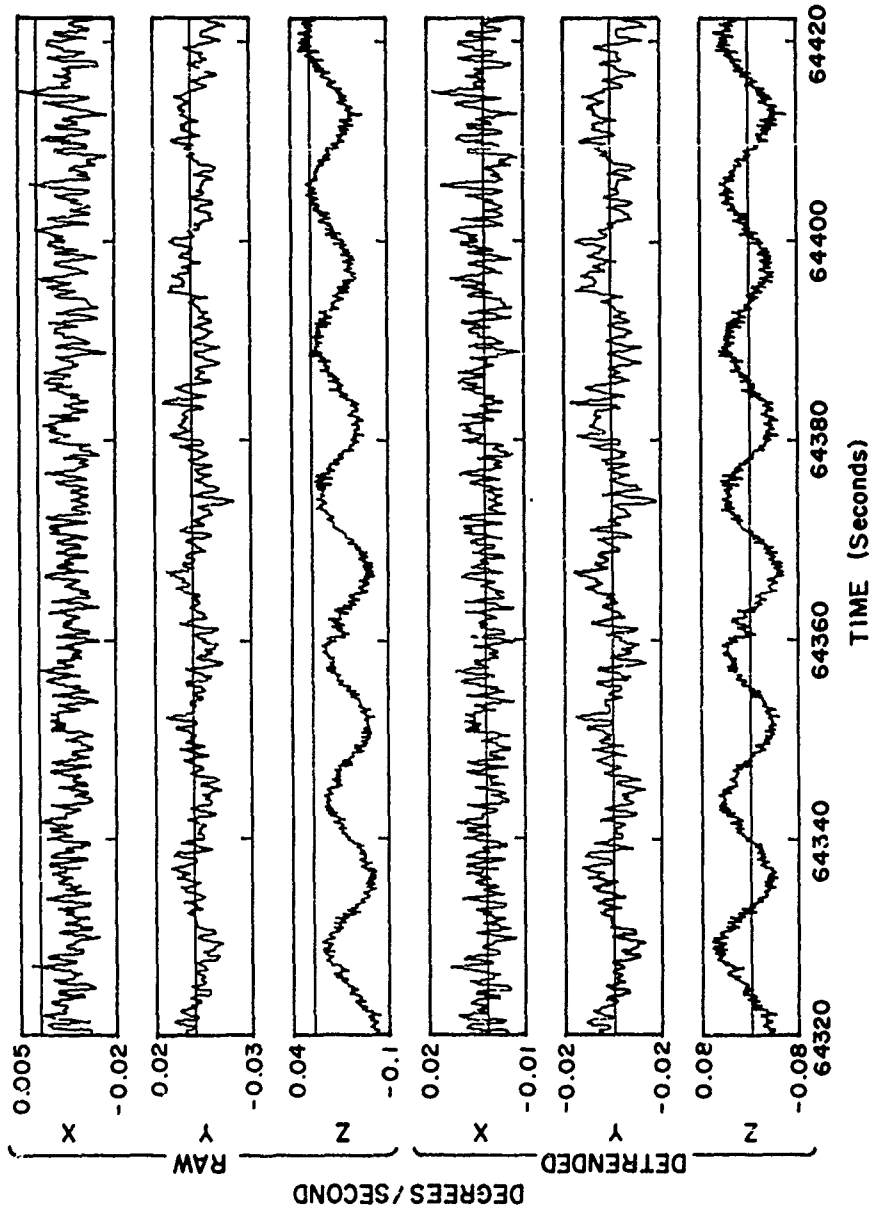


Figure 4.14 Example of Raw 3-Axis Rate Gyro Data and Detrended Version

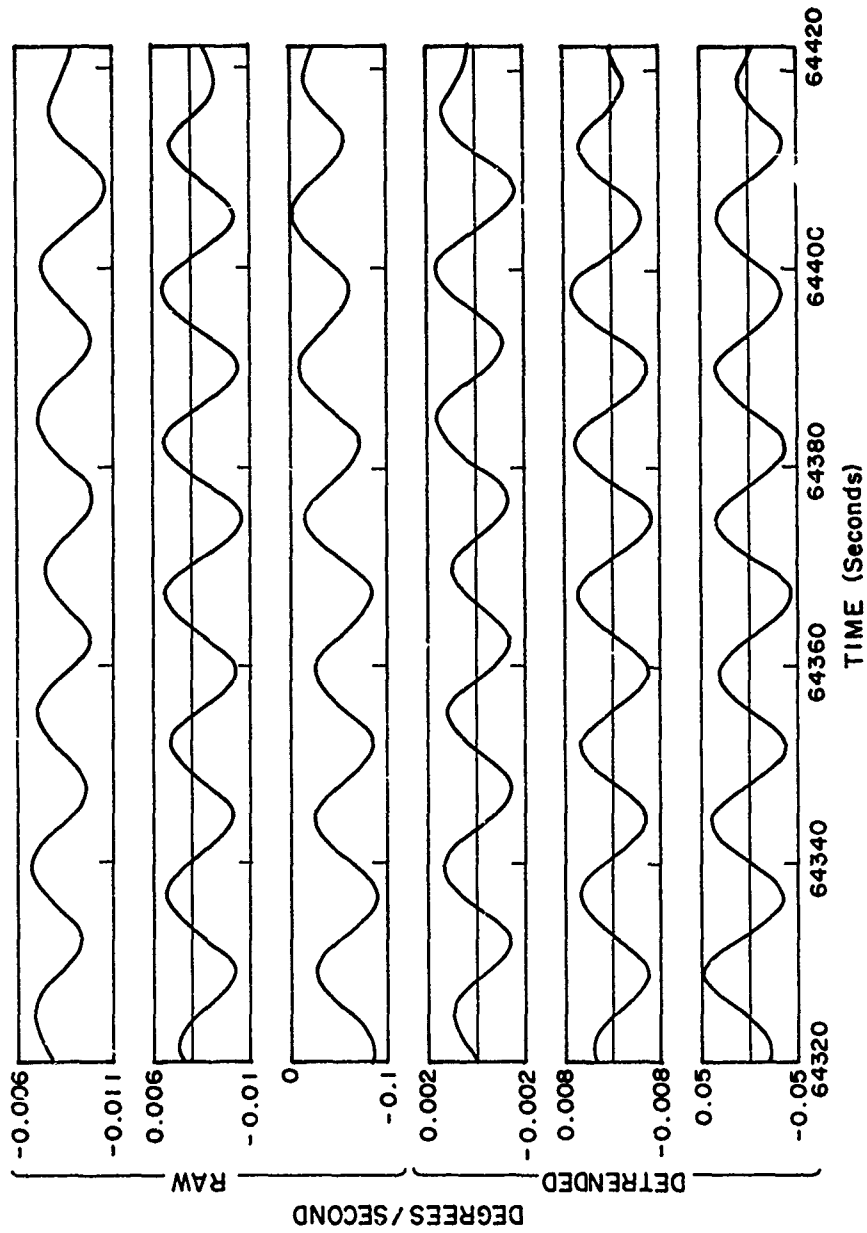


Figure 4.15 Example of Smoothed 3-Axis Rate Gyro Data and Detrended Version

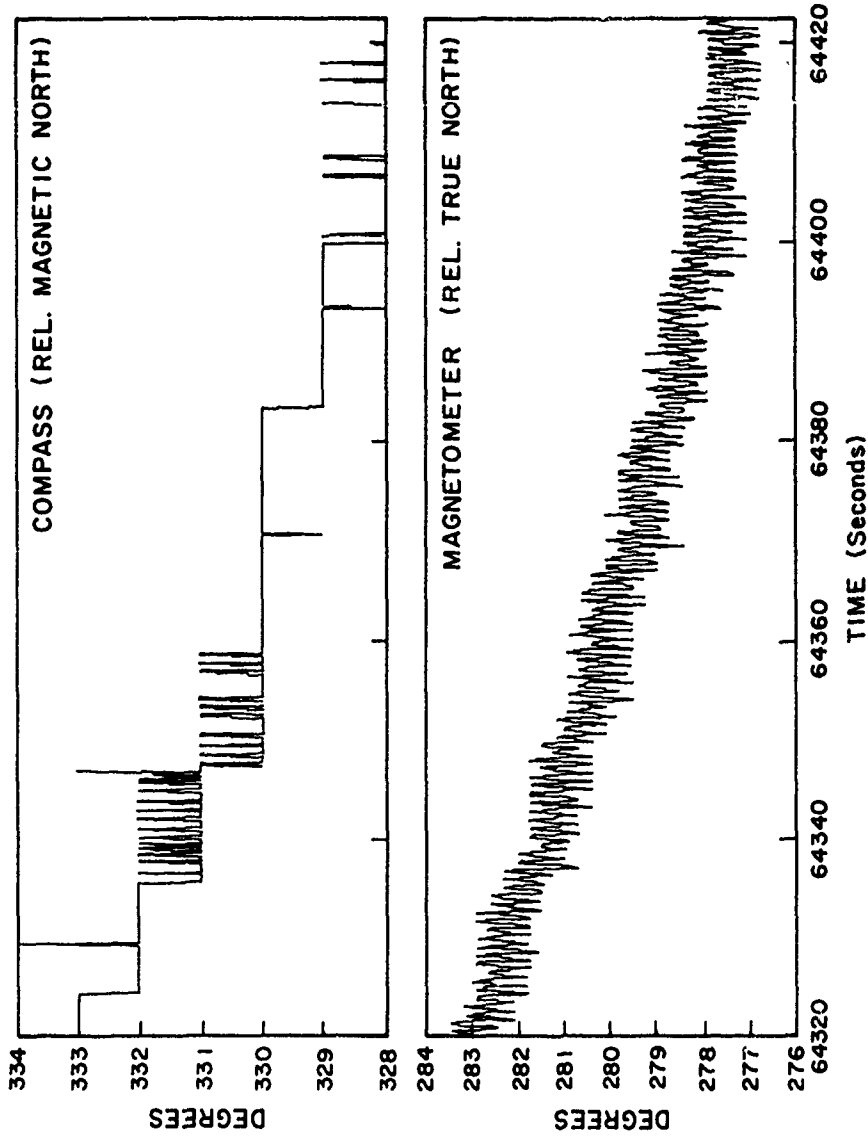


Figure 4.16 Comparison of Raw Compass Data (to Magnetic North) With Raw Magnetometer Estimate of Compass Angle (to True North). Magnetic North is about +10 deg to true North



the magnetometers. The magnetometer should show about 10-deg less than the compass due to the magnetic azimuth. There is still a 30-deg difference between the two instruments. The reason for this offset has not been determined yet. We have decided not to work this problem for this flight, at this time, but may return to it depending on the results of DUCKY II, where we expect much higher data quality. Figure 4.17 shows the residual magnetic data when the NASA MGST-481 model is subtracted (as based on the WSMR radar position data). The radial component shows a 400 nT variation. The NASA field model is only good to about 1000 km resolution, and does not account for local effects (e.g., ionospheric currents, solar activity). In addition, the magnetometers may not be calibrated to this accuracy. The  $\theta$  component will be described in more detail in the next section. The  $\phi$  component shows a vertical misalignment of about 1.35 deg with a variation of about 0.01 deg. The misalignment does not agree with the accelerometers, but the short-term variations do. Again, the magnetometer data for this component is contaminated by the same effects as for the radial component. Clearly, the magnetometer shows much promise, scientifically on its own accord, as well as for gondola-motion determination. Much remains to be resolved, however, and for now the problems will be shelved. In any case, the data set is unique scientifically, and should be looked at again.

#### Z-Rotation

Three independent sets of data are available to show the rotation of the gondola about the Z-axis: 1) compass, 2) magnetometer and 3) Z-gyro. Figure 4.18 shows the three sensors, with the integral of the Z-gyro instead of the rate data. The integrated Z-gyro data has no calibration point as this must come from either the compass or magnetometer, which do not agree. So the first integrated Z-gyro data point was defined as zero. Subtracting the three data sets in the three combinations, with an arbitrary zero point is shown in Figure 4.19. The best agreement comes from the magnetometer and integrated Z-gyro, at least for the short-term variations. We must conclude that the calibration of the compass data is suspect. but all differences and errors in rotation data are suspect as well. These data clearly need close scrutiny, but, again, have been shelved for now as the sensors for DUCKY II have been improved significantly.

#### 4.5.3 SUMMARY

In practice, the noise evident in all instruments, and the need to convert the data into an inertial frame, make this a difficult problem. Due to the difficulties and dead ends encountered in the previously described portions of this work (i.e., building a data set, analysis of translational motions), the rotational aspects have not been rigorously analyzed. This section does make the attempt to show

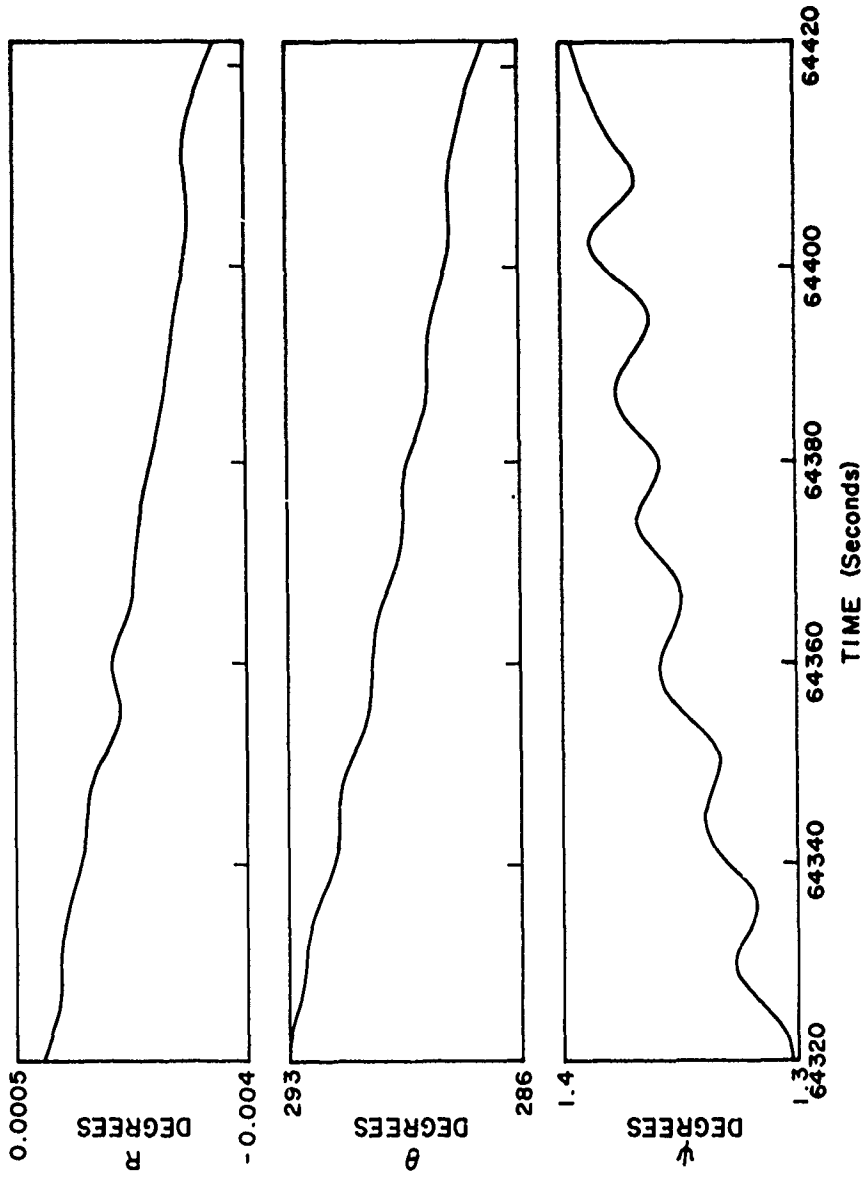


Figure 4.17 Magnetometer Data Minus NASA Magnetic Field Model in Spherical Coordinates

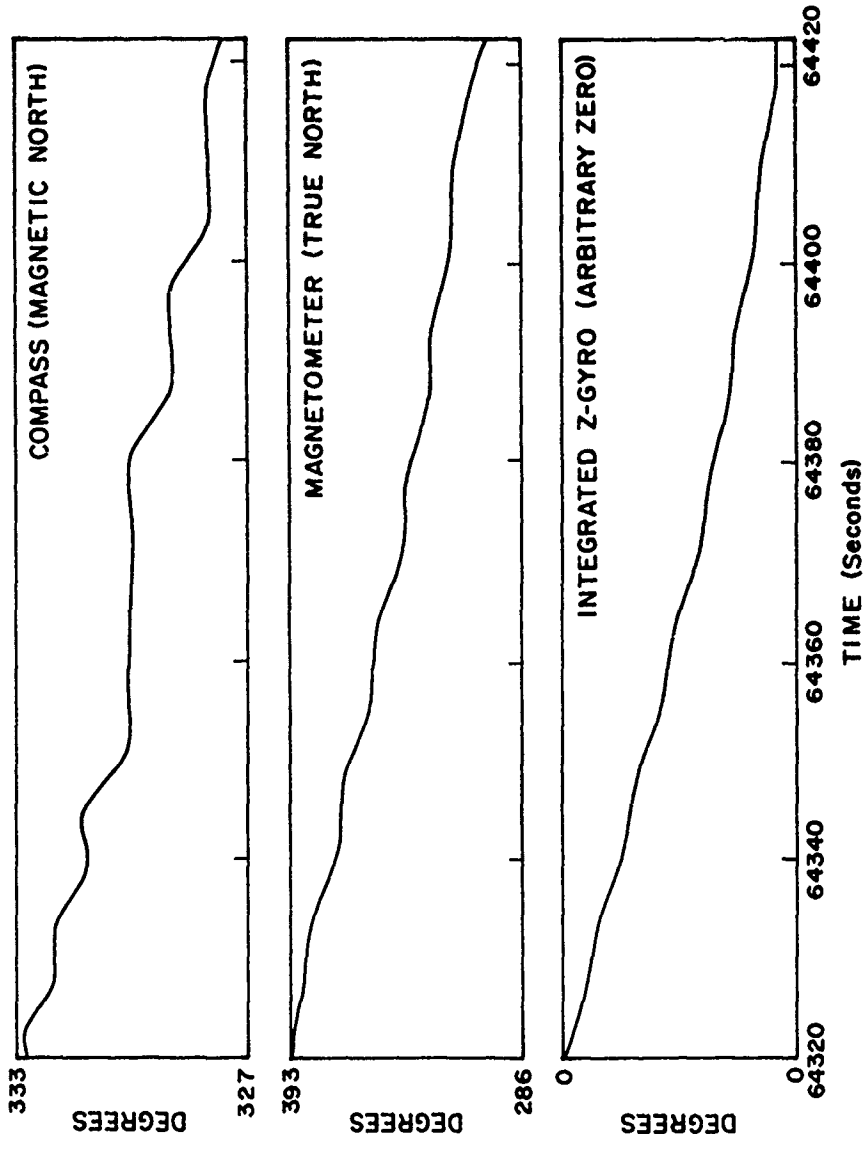


Figure 4.18 Absolute Angle About Z-Axis as Measured by (Top to Bottom) Compass, Magnetometer, and Integrated Z-Gyro (With Arbitrary Zero)

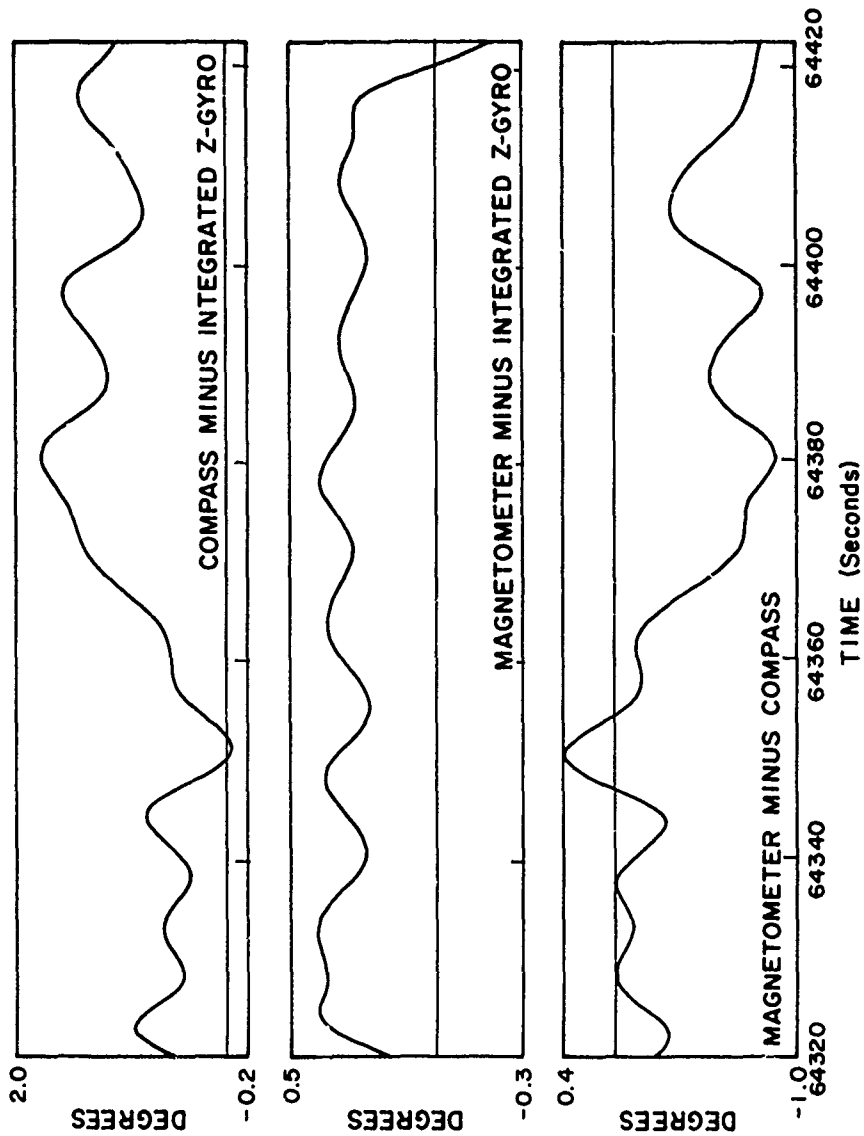


Figure 4.19 Differences Among Measurements Shown in Figure 4.18. Top to bottom: compass - integral of Z-gyro; magnetometer - integral of Z-gyro; magnetometer - compass

what insights have been gained so far in the rotational motions of the balloon-gondola system; and especially to summarize what we perceive to be necessary in subsequent flights. Sufficient information was derived from this qualitative and semi-qualitative analysis to affect the design of DUCKY II. Suggestions include: 1) Adding a swivel (rotating about the Z-axis) between the parachute and gondola. This should help uncouple rotation of the balloon (presumably driven by winds), and gondola rotation. 2) Leaving the strapdown system as is for the foreseeable future. The gondola is stable enough to consider it a stabilized platform to 0.01 deg. 3) Improving and calibrating the compass, magnetometers, and gyros.

## 5. CONCLUSIONS

### 5.1 Summary

The flight of DUCKY Ia was a complete success. All sensors worked as expected, and the data analysis has progressed well and has given valuable information for the design of future flights. This project was, and still is, a feasibility project where the goal is to design an operational instrument to measure gravity at high altitudes; that is, at about 30 km (100,000 ft). The original plan calls for two to four flights total to understand the experiment, and actually carry out gravity measurements to an accuracy of 1 mGal. For this flight, with a data analysis scheme not yet fully developed, and inadequate tracking, we feel we disagree with the DMA gravity model by  $26.5 \pm 2.5$  mGals. For a first attempt, this is a very good result.

The strategy in data analysis was to focus attention on "quiet times" where balloon and gondola motions were obviously the lowest. If necessary, the analysis could encompass the entire flight. Just the analysis of the "quiet times," however, proved sufficient to justify continuing the experiment and help redesign the system for the second flight. In particular, three issues proved more difficult than anticipated: 1) tracking, 2) rotation sensors, and 3) a total inertial navigation solution. Many approaches were tried to address these issues, and the following conclusions were reached. The radar tracking data was inadequate, and was totally dependent on flying the experiment near high-quality radar installations. It seems that the best solution is to convert to GPS tracking, and this will be done for DUCKY II. This will allow for performing the experiment anywhere on earth, independent of ground-based tracking support. Preliminary indications from other GPS experimenters suggest an order of magnitude improvement in tracking data quality. The rotation sensors were particularly sensitive to

bias and drift. Since we expect noise due to rotation to be in the tens of milligals, as this was our final error for this flight, closer attention must be paid to this issue. For the next flight, the sensitivity and calibrations for these instruments will be improved by about a factor of four. The total solution required an all-encompassing inertial navigation solution, where tracking and motion data are known, but the gravitational acceleration is not. This is a variation of typical inertial navigation systems, but is capable of being done. This part of the analysis will be submitted to the private sector for competitive bids.

Correcting for translational motion only, we find the average measured gravitational acceleration is about 30 to 35 mGals lower than expected from the models. Preliminary analysis of rotation data suggests six of those milligals can be accounted for by VSA misalignment within the gondola, and the gondola axis being misaligned with the true vertical. The misalignment is about 0.2 deg. In sum, we find our measurements are lower than expected from gravity models by about 24 to 29 mGals. We expect most of this residual error lies in noisy tracking data; instrument biases, drifts and misalignments; and incomplete data-analysis software.

An interesting concept has developed during this analysis. The data from these flights happen to fall in a potentially interesting region for General Relativity experiments. It is possible that the gravitational constant  $G$  varies with time and/or distance. Many measurements and tests have already been done, with insignificant results. No measurements have been done at the distances involved, from earth to balloon. Being the first to measure gravity in this region, we have the potential to contribute to General Relativity experiments involving  $G(r)$ . It is clear, however, that we must break the 1 mGal level, and be able to do this during ascent so we have many samples at varying distance. How well we can do this, or expect to do this, remains to be seen.

In summary, the flight and data analysis look good. We have specific improvements for subsequent flights, and we are going ahead with the project.

## References

1. Bowin, Carl O., Scheer, Eddie, and Goldsborough, Rob (1984) Technical Report - Balloon Environmental Test Report, AFGL Contractor Report.
2. Bowin, Carl, Wing, Charles G., and Aldrich, Thomas C. (1969) Test of the MIT vibrating string gravimeter, J. Geophys. Res. 74, 12:3278-3280.
3. Bowin, Carl O., Folinsbee, Allin, and Aldrich, Thomas C. (1970) Test of digital VSA sea gravity meter and comparison with LaCoste and Romberg gyrostabilized gravity meter (Abstract), Trans. Am. Geophys. Union 51, 4:261.
4. Bowin, C., Aldrich, T. C., and Folinsbee, R. A. (1972) VSA gravity meter system: tests and recent developments, J. Geophys. Res. 77:2018-2033.
5. DeLeeuw, J. H., and Kung, W. L. (1984) Development of motion-sensing package for high-altitude balloons, University of Toronto Institute for Aerospace Studies, Scientific report submitted under contract F19628-82-C-0041.
6. Makhoul, John (1975) Linear prediction: a tutorial review, Proc. IEEE 63 (No. 4).
7. Burg, John P. (1975) Maximum Entropy Spectral Analysis. Ph.D. Thesis, Stanford University.
8. Schwartz, M., and Shaw, L. (1978) Signal Processing, McGraw-Hill, New York, Ch. 7.
9. Cruz, J. Y., and Laskowski, P. (1984) Upward Continuation of Surface Gravity Anomalies, Report, 360, Dept. of Geodetic Science and Surveying, Ohio State Univ., AFGL-TR-84-0331, ADA154973.
10. Morris, A. L. (1975) Theory of balloon flight, Scientific Ballooning Handbook, NCAR-TN/IA-99, pp. II-34 to II-37.

## References (contd)

11. Iliff, Robert L., and Sands, Roger W. (1984) Relative Gravity Measurements at Holloman AFB, New Mexico, AFGL Technical Memorandum Series 95.
12. Iliff, R., and Sands, R. (1983) The AFGL Absolute Gravity Measuring System, A Final Report and Operating/Maintenance Manual, AFGL-TR-83-0297, ADA147853.
13. Marson, I., and Alasia, F. (1980) Absolute Gravity Measurements in the United States of America, AFGL-TR-81-0052, ADA099017.
14. Zumberge, M. A., Fowler, J. E., and Gschwind, J. (1983) Results from an absolute gravity survey in the United States, J. Geophys. Res. 88 (No. B9).



## LIST OF ACRONYMS

AFGL	Air Force Geophysics Laboratory
ARL	Applied Research Laboratories, University of Texas
CIGTF	Central Inertial Guidance and Testing Facility
CIRIS	Completely Integrated Range Instrumentation System
DMA	Defense Mapping Agency
FM	Frequency Modulation
GPS	Global Positioning System
I*S*P	Interactive Signal Processing (Bedford Research Associates)
MSL	Mean Sea Level
NSWC	Naval Surface Weapons Center
OSU	Ohio State University
PCM	<u>Pulse-Code Modulation</u>
PSL	Physical Sciences Laboratory, New Mexico State University
UTIAS	University of Toronto Institute for Aerospace Studies
VSA	Vibrating String Accelerometer (gravimeter)
WSMR	White Sands Missile Range
WHOI	Woods Hole Oceanographic Institute
Z-100	Zenith Z-100 microcomputer system

## Appendix A

### Relative-Gravity Measurements at Holloman AFB, New Mexico

Relative-gravity measurements were made at selected sites at Holloman AFB, NM<sup>11</sup>, in support of the AFGL balloon-borne gravity experiment. The site locations, chosen in accordance with the experiment requirements, were:

1) The Advanced Inertial Test Laboratory (AITL), Building 1256: This is an absolute site measured by AFGL/LWG in 1980,<sup>12</sup> the Instituto di Metrologia "G. Colonnetti" (IMGC) Italy in 1980,<sup>13</sup> and the Joint Institute for Laboratory Astrophysics (JILA) in 1982.<sup>14</sup> The absolute gravity marker in Room 10 in the AITL building was the starting and closing site for all measurements.

2) The High Bay, Building 850: The experiment package assembly, testing, and instrument calibration were performed in the High Bay.

3) The Altitude Test Chamber, Building 1261: Calibration data were taken here during high-altitude simulation tests.

11. Iliff, Robert L., and Sands, Roger W. (1984) Relative Gravity Measurements at Holloman AFB, New Mexico, AFGL Technical Memorandum Series 95.
12. Iliff, R., and Sands, R. (1983) The AFGL Absolute Gravity Measuring System, A Final Report and Operating/Maintenance Manual, AFGL-TR-83-0297, ADA147853.
13. Marson, I., and Alasia, F. (1980) Absolute Gravity Measurements in the United States of America, AFGL-TR-81-0052, ADA099017.
14. Zumberge, M. A., Fowler, J. E., and Gschwind, J. (1983) Results from an absolute gravity survey in the United States, J. Geophys. Res. 88 (No. B9).

4) Secondary Test Chamber, Building 1261: Due to a malfunction in the main test chamber, a secondary high-altitude simulation chamber was used for a portion of the tests. The floor of the secondary chamber is about 50 cm higher than the floor of the main chamber, so the gravity value is lower. The gravity value in the secondary chamber was calculated using the previously determined gradient of 0.285 mGal/meter.

5) Nenninger Site, Launch Pad: Measurements were made 30 m diagonally in from each of the four corners, and at the center of the launch pad. Five points were made primarily because of the relatively large gravity differences, approximately one mGal, encountered at the launch pad and the uncertainty of the launch point. Due to wind shifts, the launch point frequently is not known until just before launch.

It should be pointed out that the measurement made at the center is not at the crosspoint of the E-W/N-S reflecting markers embedded in the launch pad. These markers no longer cross at the center, due to additional lengthening of the pad in the north-south direction.

The gravity transfers were made from the AITL building with a LaCoste-Romberg G-120 meter loaned to AFGL by the Geodetic Survey Squadron (GSS). The G meter was set on its leveling feet since no disk was available. Furthermore, the meter was placed in an east-west orientation with the two leveling screws to the east, and the single screw to the west side. Three readings were made at each site and the results were corrected for earth tides, meter factor, and meter drift. Meter drift is based on constant drift from start to closure of readings.

#### Relative Measurements

The confidence level of the relative measurements is + .015mGal (except where noted).

1) AITL (Building 1256) (absolute gravity site):	979139.600 + .009 mGal
2) High Bay (Building 850):	979136.002 mGal
3) Test Chamber (Building 1261):	979136.536 mGal
4) Secondary Test Chamber:	979136.393 + 0.050 mGal
5) Nenninger Site (Launch Pad):	
a. Southeast Corner:	979140.708 mGal
b. Northwest Corner:	979141.782 mGal
c. Southwest Corner:	979141.132 mGal
d. Northeast Corner:	979141.286 mGal
e. Center of Pad:	979141.236 mGal

## Appendix B

### Gravity Model Verification PCM/FM Telemetry Data

Link No. 1    2258.5 MHz

Encoder:    Conic 410-2 S/N 1062  
Bits per Word:    10  
Bit Rate:    128 Kbits  
Output Code:    B10  
Frame Sync Pattern:    11111010111100110010  
Words per Frame:    47 (data)  
Digital Words:    3

<u>Word No.</u>	<u>Function</u>
001	Digital Word 1 (see digital bit assignments)
002	Digital Word 2 (see digital bit assignments)
003	Digital Word 3 (see digital bit assignments)
004	Not Available
005	Encoder Temperature
006	Primary Control Unit Temperature
007	Primary Command Receiver Signal Strength
008	0 - 15 PSIA Altitude Xducer
009	0 - 2 PSIA Altitude Xducer

<u>Word No.</u>	<u>Function</u>
010	0 - 0.2 PSIA Altitude Xducer
011	Primary 30-Volt Power Monitor (X8)
012	Primary 12-Volt Power Monitor (X3)
013	Accelerometer Z Axis $\pm$ 7.5g
014	Accelerometer Z Axis $\pm$ 2.5g
015	Accelerometer Y Axis $\pm$ 2.5g
016	Accelerometer X Axis $\pm$ 2.5g
017	0 Volts Calibration
018	Backup Command Receiver Signal Strength
019	Backup 30-Volt Power Monitor
020	Backup System Internal Temperature
021	Link No. 1 XMTR Temp.
022	Link No. 2 XMTR Temp.
023	AFGL Battery Section Temp.
024	UTIAS Battery Section Temp.
025	VSA Compartment Temp.
026	Digital Magnetic Compass Heading
027	Command Verification Backup System
028	Command Verification Primary System
029	Blank Tilt Sensor #113 Port and Starboard
030	Blank Tilt Sensor #114 Forward and Aft
031	UTIAS X Gyro Low Gain
032	UTIAS Y Gyro Low Gain
033	UTIAS Z Gyro Low Gain
034	UTIAS X Accelerometer Low Gain
035	UTIAS Y Accelerometer Low Gain
036	UTIAS Z Accelerometer Low Gain
037	UTIAS X Accelerometer High Gain

<u>Word No.</u>	<u>Function</u>
038	UTIAS Y Accelerometer High Gain
039	UTIAS Z Accelerometer High Gain
040	UTIAS X Magnetometer
041	UTIAS Y Magnetometer
042	UTIAS Z Magnetometer
043	UTIAS Oven Temperature
044	UTIAS Box Temperature
045	UTIAS X Gyro High Gain
046	UTIAS Y Gyro High Gain
047	UTIAS Z Gyro High Gain
048 through 062 Not Used	

DIGITAL WORD ASSIGNMENT

<u>Word No.</u>	<u>Bit No.</u>	<u>Indicated Function</u>
001	01	Flight Time Remaining Tens -2 <sup>3</sup>
	02	Flight Time Remaining Tens -2 <sup>2</sup>
	03	Flight Time Remaining Tens -2 <sup>1</sup>
	04	Flight Time Remaining Tens -2 <sup>0</sup>
	05	Flight Time Remaining Units -2 <sup>3</sup>
	06	Flight Time Remaining Units -2 <sup>2</sup>
	07	Flight Time Remaining Units -2 <sup>1</sup>
	08	Flight Time Remaining Units -2 <sup>0</sup>
	09	Termination by Primary
	10	Termination by Backup
002	01	CMD19 POWER CONTROL INDICATOR WHOI PRIMARY
	02	CMD19 POWER CONTROL INDICATOR WHOI BACKUP
	03	CMD15 POWER CONTROL INDICATOR UTIAS PRIMARY
	04	
	05	
	06	
	07	
	08	
	09	
	10	
003	01	Ballast Pour
	02	Not Used
	03	Not Used
	04	Helium Valve Open
	05	Burst Switch Armed
	06	Burst Pin Pulled Above 10Kft
	07	Burst Pin Pulled Above 10Kft
	08	Not Used
	09	Not Used
	10	Not Used

GRAVITY MODEL VERIFICATION  
PCM/FM TELEMETRY DATA

Link No. 2

2279.5 MHz

Encoder: 20K-32 (Lab Built)  
 Bits per Word: 10  
 Bit Rate: 19.2 kHz Fixed  
 Output Code: B10  
 Frame Sync Pattern: 11101101111000100000  
 Words per Frame: 30 - 27 Analog - 3 Digital

<u>Word No.</u>	<u>Function</u>
001	Digital Word 1
002	Digital Word 2
003	Digital Word 3
004	Plate Temp
005	Heat Sink Temp
006	Outer Can Temp
007	Inner Can Temp
008	Outer Can Control Voltage
009	Inner Can Control Voltage
010	Outer Can Power
011	Inner Can Power
012	Battery Voltage
013	Chamber Temp
<hr/> <u>All following words are repeats of above words</u>	
014	Cardcage Temp
015	Outer Can Temp
016	Inner Can Temp
017	Outer Can Control Voltage
018	Inner Can Control Voltage
019	Outer Can Power



GRAVITY MEASUREMENTS FLIGHT H83-19  
STRIP CHART DATA RECORDING ASSIGNMENTS

<u>Recorder #1</u>	Link #1	Word
Primary RCVR Sig Strength		007
Backup RCVR Sig Strength		018
Command Verify Primary		028
Command Verify Backup		027
Digital Mag Compass		026
Z Accel $\pm 7.5g$		013
Z Accel $\pm 2.5g$		014
Time Code		

<u>Recorder #2</u>	Link #1	Word
Z Accel Low Gain		036
Z Accel High Gain		039
X Accel Low Gain		034
X Accel High Gain		037
Y Accel Low Gain		035
Y Accel High Gain		038
Time Code		

<u>Recorder #3</u>	Link #2	Word
Flat Plate Temp		004
Heat Sink Temp		005
Outer Can Temp		006
Outer Can Control Volts		008
Outer Can Power		010
Inner Can Temp		007
Inner Can Control Volts		009
Inner Can Power		011

<u>Recorder #4</u>	Link #1	Word
X Gyro Low Gain		031
X Gyro High Gain		045
Y Gyro Low Gain		032
Y Gyro High Gain		046
Z Gyro Low Gain		033
Z Gyro High Gain		047
Time Code		

<u>Recorder #5</u>	Link #1	Word
Digital Mag Compass		026
Tilt Port/Starboard		029
Tilt Forward/Aft		030
Z Magnetometer UTIAS		042
Z Accel $\pm 2.5g$		014
Time Code		

## Appendix C

### Gravity Preload Preflight Schedule

<u>IN HIGH BAY (NIGHT OF LAUNCH)</u>		<u>TIME</u> completed
UTIAS install ice pack	30 min	0030
WHOI install front plate VSA section	10	0040
AFGL install batteries	20	0100
(Note: parachute will be in flight trim and final rigging at the triplate)		
AFGL run preliminary flight line checks	30	0130
(Refer to High Bay Checklist)		
AFGL install 1-in. insulators, web belts, etc.	10	0140
WHOI perform level tests	30	0210
AFGL complete High Bay checks		
AFGL ensure VSA and battery sections doors in place		
AFGL power down except for WHOI		
AFGL remove auxiliary battery connector		
AFGL secure turnbuckles with safety wire	30	0240
AFGL install all doors and insulation with straps		

TURN OVER SYSTEM TO CREW CHIEF FOR WEIGHOFF AND TRANSPORT TO  
NENNINGER SITE

60

0340

AT LAUNCH SITE

AFGL remove battery compartment door

WSMR perform transponder tests

AFGL do control center tests (Refer to Flight Line Checklist)

AFGL get data report from TM re sensors status

WHOI record data for 15 min

60

0440

Prepare for final rigging of parachute to balloon

AFGL turn power off manually using package start box

Launch crew lay out balloon and parachute

Connect parachute to balloon and check payload release device and burst switch  
installation

Check all connections among gondola, parachute, and balloon

Reapply power to system

Remove WHOI battery pack

Remove start box

Close door

Insulate gondola

45 min

0525

Final weighoff scale check

15

0540

PERMISSION TO LAUNCH

0600

## Appendix D

### Control Center Log

H83-19  
Gravity

Time (GMT)	
0515	WX is go. Mission is go. Recording updated.
0700	Control Center opened.
0901	Launch Crew departing for Nenninger Site.
0944	Launch Crew at Nenninger Site.
0955	Laying out Bubble.
1003	Inflation pressure confirmed.
1013	Beginning balloon layout.
1035	Balloon layout complete.
1100	Holding for winds.
1309	Trouble with radios; all parties requested to go to F2 and stay there.
1320	Still holding - winds.
1341	Starting inflation.
1400	Approximately 15 minutes to launch.
1409	Clearance to launch.
1411.29	LAUNCH.
1417	CR/R and three radars OJ this time.
1418	Balloon at 10Kft.
1431	Balloon at 20Kft.
1452	Balloon at 40Kft; heading SE at 112 knots.
1504	FH13 called in; will call back at 1615.
1528	Balloon at 70Kft.
1555	FH60 heading to Hobbs.
1604	Balloon at float.
1609	F13 heading at Hobbs Airport. HF check showed 5707.0kHz worked. Heard 60 weak, but could understand what they said.

1708 FH13 called, standing by at Airport; PH 393-9275  
 1804 BS disarmed.  
 1805 Valve opened.  
 1826 FH13 called, standing by. FH60 will call in ½ hour, 1900Z.  
 1828 Valve closed.  
 1857 FH13 called; FH60 will get airborne and stay in Hobbs vicinity;  
 FH 13 will stand by.  
 1907 Balloon at 85.8KFT and dropping slowly.  
 1908 Pouring 90 sec of ballast.  
 1921 Pouring 45 sec of ballast.  
 1929 Pouring 20 sec of ballast.  
 1933 Termination NOTAM given (-1 hour).  
 2000 FH60 in the air.  
 2009 Pouring 20 sec of ballast.  
 2017 FH13 heading to west side of Hobbs on Hwy 180/62.  
 2025 5 min to termination.  
 2030 TERMINATION!  
 2032 Balloon past chute.  
 2037 Payload at 60K.  
 2040 Payload at 55K.  
 2045 Payload at 45K.  
 2046 Balloon impact; 080° 51.5 nm Earlstrad VOR.  
 100° 57 nm Roswell VOR.  
 2051 Payload at 35K, loss of radar.  
 2054 FH60 lost payload in clouds.  
 2059 Payload at 25K.  
 2106 Pouring ballast.  
 2107 TM loss.  
 2116 Pour command dropped.  
 2119 13 and 60 have a visual, payload at approx 7K.  
 2124 Payload Impact: 084° 11.5 nm Hobbs VOR.  
 300° 57 nm Midland VOR.  
 2146 Recovery at site.  
 2311 Picked up payload, heading to Airport to drop. Lt. DePiero off  
 with 60, then picked up balloon.  
 CLOSING DOWN.

## **REPRODUCTION QUALITY NOTICE**

**We use state-of-the-art high speed document scanning and reproduction equipment. In addition, we employ stringent quality control techniques at each stage of the scanning and reproduction process to ensure that our document reproduction is as true to the original as current scanning and reproduction technology allows. However, the following original document conditions may adversely affect Computer Output Microfiche (COM) and/or print reproduction:**

- **Pages smaller or larger than 8.5 inches x 11 inches.**
- **Pages with background color or light colored printing.**
- **Pages with smaller than 8 point type or poor printing.**
- **Pages with continuous tone material or color photographs.**
- **Very old material printed on poor quality or deteriorating paper.**

**If you are dissatisfied with the reproduction quality of any document that we provide, particularly those not exhibiting any of the above conditions, please feel free to contact our Directorate of User Services at (703) 767-9066/9068 or DSN 427-9066/9068 for refund or replacement.**

**END SCANNED DOCUMENT**